




Article

Electrochemical Activation of Li_2MnO_3 Electrodes at 0°C and Its Impact on the Subsequent Performance at Higher Temperatures

Francis Amalraj Susai ¹, Michael Talianker ², Jing Liu ³, Rosy ¹, Tanmoy Paul ⁴, Yehudit Grinblat ¹, Evan Erickson ¹, Malachi Noked ¹, Larisa Burstein ⁵, Anatoly I. Frenkel ⁶, Yoed Tsur ⁴, Boris Markovskiy ^{1,*} and Doron Aurbach ^{1,*}

¹ Department of Chemistry and Institute of Nanotechnology and Advanced Materials, Bar-Ilan University, Ramat-Gan 52900, Israel; sfamalraj@gmail.com (F.A.S.); rrosysharma@gmail.com (R.S.); Judith.Grinblat@biu.ac.il (Y.G.); evan.m.erickson@gmail.com (E.E.); malachi.noked@biu.ac.il (M.N.)

² Department of Materials Engineering, Ben-Gurion University of the Negev, Beer-Sheva 84105, Israel; mtalianker973@gmail.com

³ Department of Physics, Manhattan College, Riverdale, New York, NY 10471, USA; jing.liu@huskers.unl.edu

⁴ Department of Chemical Engineering and the Grand Technion Energy Program, Technion-Israel Institute of Technology, Haifa 3200003, Israel; tanmoykent@gmail.com (T.P.); tsur@technion.ac.il (Y.T.)

⁵ The Wolfson Applied Materials Research Centre, Tel-Aviv University, Tel-Aviv 69978, Israel; bursten@tauex.tau.ac.il

⁶ Department of Materials Science and Chemical Engineering, Stony Brook University, Stony Brook, New York, NY 11794, USA; frenkel@bnl.gov

* Correspondence: markovskiyboris22@gmail.com (B.M.); Doron.Aurbach@biu.ac.il (D.A.)

Received: 6 September 2020; Accepted: 24 September 2020; Published: 1 October 2020



Abstract: This work continues our systematic study of Li- and Mn- rich cathodes for lithium-ion batteries. We chose Li_2MnO_3 as a model electrode material with the aim of correlating the improved electrochemical characteristics of these cathodes initially activated at 0°C with the structural evolution of Li_2MnO_3 , oxygen loss, formation of per-oxo like species (O_2^{2-}) and the surface chemistry. It was established that performing a few initial charge/discharge (activation) cycles of Li_2MnO_3 at 0°C resulted in increased discharge capacity and higher capacity retention, and decreased and substantially stabilized the voltage hysteresis upon subsequent cycling at 30°C or at 45°C . In contrast to the activation of Li_2MnO_3 at these higher temperatures, Li_2MnO_3 underwent step-by-step activation at 0°C , providing a stepwise traversing of the voltage plateau at $>4.5\text{ V}$ during initial cycling. Importantly, these findings agree well with our previous studies on the activation at 0°C of $0.35\text{Li}_2\text{MnO}_3\cdot 0.65\text{Li}[\text{Mn}_{0.45}\text{Ni}_{0.35}\text{Co}_{0.20}]\text{O}_2$ materials. The stability of the interface developed at 0°C can be ascribed to the reduced interactions of the per-oxo-like species formed and the oxygen released from Li_2MnO_3 with solvents in ethylene carbonate–methyl-ethyl carbonate/ LiPF_6 solutions. Our TEM studies revealed that typically, upon initial cycling both at 0°C and 30°C , Li_2MnO_3 underwent partial structural layered-to-spinel ($\text{Li}_2\text{Mn}_2\text{O}_4$) transition.

Keywords: lithium-ion batteries; Li- and Mn-rich materials; Li_2MnO_3 activation at 0°C ; stabilized cycling; decreased the voltage hysteresis; layered-to-spinel transition; bulk and surface characteristics

1. Introduction

Among various materials for cathodes for advanced Li-ion batteries (LIB), Li- and Mn- rich oxides like $\text{Li}_{1+x}\text{Ni}_y\text{Co}_z\text{Mn}_{0.5+w}\text{O}_2$ ($x + y + z + w = 0.5$) or $x\text{Li}_2\text{MnO}_3\cdot(1-x)\text{LiMO}_2$ ($M = \text{Mn}, \text{Ni}, \text{Co}$) are the most promising because of their high discharge capacity ($>250\text{ mAh/g}$) after the first activation

charge–discharge cycle and high energy density, i.e., ~1000 Wh/kg. These materials have attracted much attention since they were first synthesized and introduced by Thackeray et al. [1–7]. It should be emphasized that during the last decade, sodium and potassium ion batteries—in which the energy storage mechanism is similar to that in LIBs—have been proposed and studied worldwide [8–14]. Electrodes comprising high-energy lithiated Ni, Co, Mn oxides (HE-NCM) suffer from fast capacity fading, large voltage hysteresis, and transition metal dissolution during prolonged cycling [5,15–25]. Therefore, researchers have proposed several approaches to stabilize their electrochemical performance, such as surface coatings by oxides and salts, for instance Al_2O_3 , TiO_2 , ZrO_2 , AlF_3 [26–28], cationic or anionic lattice doping with Na^+ , Mg^{2+} , Al^{3+} , F^- , etc. [29–33], and gas treatment at high temperature with NH_3 , SO_2 , CO_2 , or F_2 [34–37]. Additionally, Thackeray et al. [38,39] showed that treatment of HE-NCM materials with inorganic acids (H_2SO_4 , HNO_3) resulted in stable electrochemical behavior. We recently demonstrated [40] that stable cycling and higher rate capability and lower voltage hysteresis of HE-NCM cathodes in Li-cells can be achieved after the treatment of these materials with trimesic or terephthalic acids at 600 °C. An important finding was reported in our previous work [41], i.e., that performing initial (activation) cycling of HE-NCM electrodes at low temperature, for instance at 0 °C or at 15 °C, resulted in higher discharge capacity and decreased and stabilized voltage hysteresis compared to electrodes initially activated and cycled at the higher temperatures (e.g., 30° and 45 °C). In that work, we used $0.35\text{Li}_2\text{MnO}_3 \cdot 0.65\text{Li}[\text{Ni}_{0.35}\text{Mn}_{0.45}\text{Co}_{0.20}]\text{O}_2$, a material referred as a two-phase system consisting of layered, structurally compatible components: Li_2MnO_3 (monoclinic, space group $C2/m$) and $\text{Li}[\text{Ni}_{0.35}\text{Mn}_{0.45}\text{Co}_{0.20}]\text{O}_2$ (rhombohedral, space group $R-3m$) integrated on a nanoscale [15,18,42–44] and demonstrating common d -spacing [45]. Li_2MnO_3 is attracting attention not only as one of the end-members of the HE-NCM materials, but as a high-capacity cathode with a theoretical capacity of ~460 mAh/g for total Li extraction when charged to potentials >4.6 V. However, Li_2MnO_3 can provide high specific capacity (>200 mAh/g) only in electrodes comprising nanosized particles which demonstrate higher capacity and enhanced cycling behavior, compared to those of submicronic or micron-sized materials. Li_2MnO_3 plays a critical role in HE-NCM cathodes, providing high capacity during cycling in the potential range of 2.0–4.6 V by introducing a reversible anionic red-ox chemistry, $2\text{O}^{2-} \rightarrow \text{O}_2^{2-} + 2\text{e}^-$ (in the framework of the crystal structure of the oxide). This oxygen redox compensates for almost half of the measured capacity of HE-NCMs in the initial cycles, and more than one-third of the capacity results from reversible oxygen redox after 70 cycles, as established by Tarascon et al. [45]. Despite the numerous experimental [46–52] and theoretical [53–57] studies on Li- and Mn-rich layered materials as cathodes in Li-cells, much effort is still required to reveal the relationship among the composition of these materials and their structure, layered-to-spinel phase transformations, and enhanced electrochemical characteristics, depending on the cycling conditions (e.g., potential window, current density applied), electrolyte solutions, and temperature.

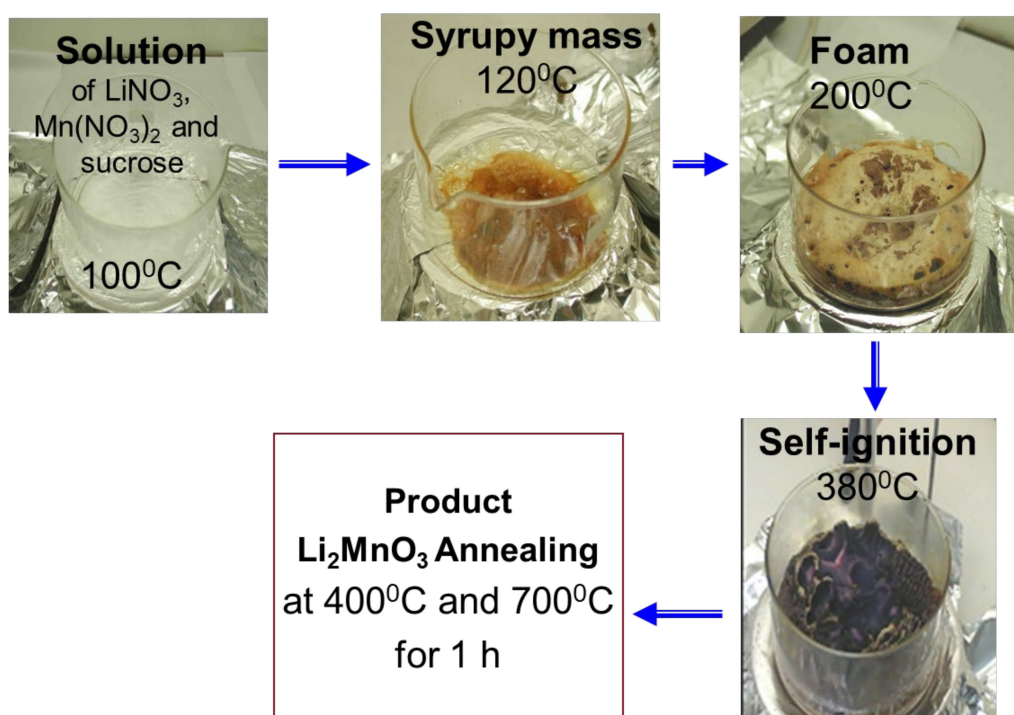
The main goal of the present work, which is a continuation of our recent research [41], was to study how the initial (activation) cycling of Li_2MnO_3 electrodes at low temperature (0 °C) influences their subsequent electrochemical performance at the higher temperatures (for instance, 30 °C and 45 °C). We also aimed to correlate the improved electrochemical characteristics of these electrodes—i.e., in terms of their stabilized capacity and voltage hysteresis—with the structural evolution of Li_2MnO_3 , oxygen loss, the formation of per-oxo like species $(\text{O}_2)^{n-}$, and a problematic surface chemistry. Thus, we hoped to gain a deep understanding of the basic phenomenon of the temperature-dependent activation (“low-T activation”) of $x\text{Li}_2\text{MnO}_3 \cdot (1-x)\text{Li}[\text{Ni-Mn-Co}]\text{O}_2$ materials at 0 °C.

2. Materials and Methods

2.1. Synthesis of Li_2MnO_3

Li_2MnO_3 was produced by solution-combustion reaction (SCR) using an aqueous solution of lithium nitrate (LiNO_3) and manganese nitrate ($\text{Mn}(\text{NO}_3)_2$) (Sigma-Aldrich, St. Louis, MO, USA), which acted as the oxidant, and sucrose $\text{C}_{12}\text{H}_{22}\text{O}_{11}$ as the fuel, similarly to previous reports [58,59].

The oxidant/fuel ratio was 1:1. Below, we present Scheme 1, which illustrates the process of the SCR. First, by heating the solution of lithium and manganese nitrates and sucrose to 100 °C, the water evaporated slowly and the mixture transformed into a syrupy mass. At ~200 °C, foam was formed and further heating led to the self-ignition of the reactants. The obtained product was amorphous; to obtain a well-crystallized Li_2MnO_3 , the as-prepared material was ground with pestle and mortar and annealed in an aluminum crucible at 400 and 700 °C for 1 h in air. The individual primary particles obtained were of 30–100 nm in size, some of which were agglomerates of ~1–1.5 μm . A SEM image is presented in Figure S1. The specific active surface area was ~20 $\text{m}^2 \text{g}^{-1}$, as measured by the Brunauer, Emmet and Teller (BET) method (Gemini 2375, Micromeritics, multipoint mode). Chemical analysis of the annealed product was carried out using the inductive coupled plasma technique (ICP-AES, spectrometer Ultima-2 from Jobin-Yvon Horiba, Montpellier, France). The composition of the material was Mn:Li = 1:2, corresponding to Li_2MnO_3 , with a measurement accuracy of ~98%.



Scheme 1. Self-combustion synthesis of Li_2MnO_3 from Li- and Mn-nitrates (oxidants) and sucrose (fuel).

2.2. Preparation of Electrodes and Electrochemical Cells

Working electrodes (cathodes) for electrochemical cells were prepared by mixing the active material Li_2MnO_3 with carbon black super P (from Timcal, Bodio, Switzerland), graphite KS-6 (Timcal, Bodio, Switzerland) and polyvinylidene difluoride binder PVdF (Solef 5130 from Solvay, Brussels, Belgium) at a ratio of 80:10:10 wt.%, in N-methyl pyrrolidone (Sigma-Aldrich, St. Louis, MO, USA) using a Thinky (Tokyo, Japan) planetary vacuum mixer to obtain a slurry. It was then cast onto an aluminum foil (15 μm thick, from Strem chemicals, Newburyport, MA, USA), dried on a hotplate, followed by drying at 120 °C under vacuum overnight.

2.3. Electrochemical Measurements

Electrochemical tests were carried out in two-electrode cells of 2325 coin-type configuration (parts from NRC-CNRC, Ottawa, Ontario, Canada). The geometric area of the working electrodes was ~1.5 cm^2 , and the average loading of the active mass was ~3 mg/cm^2 . Counter electrodes were prepared from ~200- μm thick lithium foil (Honjo metal Co., Osaka, Japan). Electrochemical cells were assembled in a glove box (VAC, from Hawthorne, CA, USA) filled with highly pure argon (5N,

Maxima, Ashdod, Israel). The electrolyte solutions (Li battery grade, LP57 from BASF, Ludwigshafen, Germany) comprised 1M LiPF₆ dissolved in ethyl-methyl carbonate (EMC) and ethylene carbonate (EC), at a weight ratio 7:3. For statistical purposes, we studied the electrochemical performance of at least 2–3 cells simultaneously, and the results were averaged. The electrochemical measurements were performed using a multichannel Maccor-2000 battery cycler and a battery test unit model 1470, coupled with a frequency response analyser (FRA) model 1255 from Solartron, Inc, Shildon, Durham, UK, driven by Corrware and ZPlot software (from Scribner Associates, Inc., Southern Pines, NC, USA). The alternating voltage amplitude in impedance measurements was 3 mV and the frequency ranged from 100 kHz to 5 mHz. The electrochemical impedance spectroscopy data were analyzed using Impedance Spectroscopy Genetic Programming (ISGP), a matlab based program that finds the distribution function of relaxation times (DFRT) via genetic programming [60–62]. ISGP finds an analytical form of the DFRT, which makes it possible to follow the changes in each peak that ideally represent a process. All the potentials in this paper are given vs. Li⁺/Li. Electrochemical tests and online electrochemical mass spectrometry measurements were conducted in thermostats at 0 °C (from Binder, GmbH-Tuttlingen, Germany) and higher temperatures (from MRC, Holon, Israel).

2.4. Structural and Surface Studies

X-ray powder diffraction (XRD) (Billerica, MA, USA) measurements were performed in the 2 θ range from 10 to 80°, with a step size of 0.02° at 15 sec/step rate. Analysis of the XRD patterns was carried out using the PowderCell program [63] and the Fullprof program, as described elsewhere [64]. Transmission electron microscopy (TEM) studies of the Li₂MnO₃ particles were performed with a LaB₆-200 kV Jeol-2100 electron microscope (Tokyo, Japan), and convergent beam electron diffractions (CBED) were taken using a 7-nm probe size. Samples for the TEM studies were prepared by the methodology described in [65]. Scanning electron microscopy (SEM) images of Li₂MnO₃ powder were obtained using E-SEM (environmental scanning electron microscope), Quanta FEG (Thermo Fisher Scientific, Agawam, US). Micro-Raman spectroscopy measurements of electrodes and powders scratched from them were performed at room temperature using a micro-Raman spectrometer from Renishaw inVia (Banbury, UK) equipped with a 514 nm laser, a CCD camera, and an optical Leica microscope. A 50 \times objective lens to focus the incident beam and an 1800 lines/mm grating were used. For statistical purposes, Raman spectra were recorded from 10–20 locations arbitrarily chosen on a sample. X-ray Photoelectron Spectroscopy (XPS) measurements were performed in ultrahigh vacuum (2.5×10^{-10} Torr base pressure) using a 5600 Multi-Technique System (Physical Electronics Inc, MN, USA). The samples were irradiated with an Al K α monochromated source (1486.6 eV) and the outcome electrons were analyzed by a spherical capacitance analyzer using the slit aperture of 0.8 mm in diameter. High resolution spectra were taken at pass energy of 11.75 eV at increments of 0.05 eV/step to allow precise energy position and peak shape determination. Curve fitting was done with a Gaussian-Lorentzian function using the 5600 Multi-Technique System software (from PHI, Buras, LA, USA). Mn K-edge X-ray absorption fine structure (XAFS) spectroscopic measurements of Li₂MnO₃ were carried out at BL2-2 beamline at Stanford Synchrotron Radiation Light source (SSRL) in transmission mode. The Li₂MnO₃ sample was ground to a fine powder and brushed on tape for measurements. XAFS data processing and analysis were done using the Athena and Artemis software within the IFEFFIT package [66]. The normalized k^2 -weighted EXAFS data were Fourier transformed in a k range of 2–11 Å⁻¹ for Mn. In the fits, the contributions from two metal–oxygen (M–O) paths with different interatomic distance and one metal–metal (M–M) path according to the Li₂MnO₃ structure were included. The value of the amplitude reduction factor (S_0^2) was obtained from the fitting of the pristine Li₂MnO₃ powder and fixed in the fits of the electrode materials.

2.5. Online Electrochemical Mass Spectrometry

A customized online electrochemical mass spectrometer (OEMS) with a multi-inlet capillary system (Hiden Analytical, Warrington, UK) was used to analyze the evolving gases, in operando, as a function

of the applied potential and temperature. A laboratory-made cell for the OEMS measurement was assembled inside an Argon filled glovebox with Li_2MnO_3 as the cathode (\varnothing 10 mm), Li foil as the anode (\varnothing 14 mm), and 100 μL LP 57 as the electrolyte solution. Two polyethylene separators (\varnothing 29 mm) were placed between the cathode and anode. The cell was connected to OEMS through a microcapillary using one of the Swagelok valves located at the head part of the cell. A vacuum of 10^{-6} torr was maintained while sampling the evolved gases at a rate of 12 $\mu\text{L/s}$. The electrochemical measurements were carried out using VSP-potentiostat (Bio-logic Science instruments, Seyssinet-Pariset, France) in a potential window of 2.4–4.7 V. The variation of desired gases with time was investigated using Mid mode. The measurements were carried out at 0° and 30°C using thermostats.

3. Results and Discussion

3.1. Structural and Morphological Characteristics of Li_2MnO_3

Figures S1 and S2, respectively, represent the SEM image of the Li_2MnO_3 particles measured from the as-prepared annealed product and its XRD profile. It can be seen in Figure S1 that the size of the primary particles varies between 30 and 100 nm, with some forming submicronic and micron-sized aggregates. The XRD pattern in Figure S2 shows peak positions characteristic of the Li_2MnO_3 phase that correspond to the $C2/m$ symmetry, including weak overlapping peaks (020) and (110) at $2\theta = 20 - 22^\circ$, which arose due to the ordering in the transition metal layers comprising Li and Mn ions in an atomic ratio 1:2. This is in accordance with the approach describing the monoclinic Li_2MnO_3 structure [67,68] as a layered compound similar to LiMO_2 , thus representing the formula Li_2MnO_3 in layered notation as $\text{Li}[\text{Li}_{1/3}\text{Mn}_{2/3}]\text{O}_2$, while the ordered $[\text{Li}_{1/3}\text{Mn}_{2/3}]$ layers are stacked along the c -axis.

The unit cell parameters of the monoclinic phase as calculated from the XRD data (reliability factor of $R_p = 2.55\%$) are as follows: $a = 4.926 \text{ \AA}$, $b = 8.512 \text{ \AA}$, $c = 5.022 \text{ \AA}$, $\beta = 109.33^\circ$, which is in line with the values reported in the literature [68]. The results of TEM analysis are consistent with the structural information obtained by XRD. A TEM image of individual particles of the annealed, as-synthesized material is represented in Figure 1 with an insert showing the CBED pattern, which was taken from the particle indicated with an arrow and indexed on the basis of its monoclinic Li_2MnO_3 structure. A small region of this particle was also used to obtain a high-resolution image shown in Figure S3. As expected, the distances measured between the atomic planes were 0.43 nm and 0.41 nm, thus matching, respectively, the interplanar spacings d_{020} and d_{110} in the monoclinic Li_2MnO_3 structure. Furthermore, Fourier transform (see insert) of a part of the image looks exactly the same as the CBED pattern (Figure 1) recorded in the diffraction experiment.

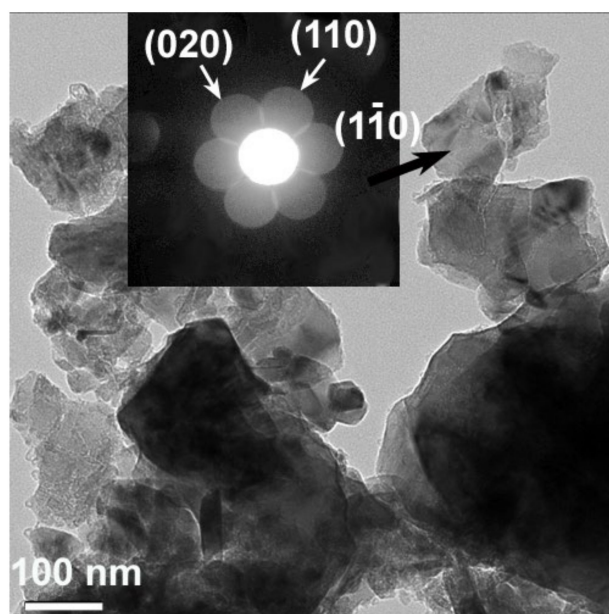


Figure 1. Bright field TEM image of the particles of pristine Li₂MnO₃ material. The insert shows an example of CBED pattern, which was taken from the particle indicated by an arrow. The pattern was indexed on the basis of the monoclinic Li₂MnO₃ structure.

3.2. Electrochemical Behavior and Structural Evolution of Li₂MnO₃ Electrodes at 0 °C, 30 °C, and 45 °C. Impact of their Initial Activation Cycling at 0 °C

In Figure 2a–c, we compare the voltage profiles measured during the initial galvanostatic charge–discharge cycles from Li₂MnO₃ electrodes at 0 °C, 30 °C and 45 °C, respectively. The first charging processes for all of these electrodes up to 4.7 V were characterized by a steep potential increase in the potential range from OCV to ~4.4–4.5 V, at which Li₂MnO₃ was electrochemically inactive, followed by an irreversible potential plateau related to the Li₂MnO₃ activation and the Li⁺ deintercalation, in agreement with the literature reports [48,49]. It is important to note that upon the initial charge reaction, the potential plateaus were registered at 4.66 V, 4.60 V, and 4.55 V for the above Li₂MnO₃ electrodes at 0 °C, 30 °C, and 45 °C, respectively. This observation is in line with our finding in a previous study [41], in which Li₂MnO₃-including Li- and Mn-rich electrodes 0.35Li₂MnO₃·0.65Li[Mn_{0.45}Ni_{0.35}Co_{0.20}]O₂ at 0 °C exhibited the 1st charging voltage plateau at ~4.7 V that was 150–200 mV higher compared to those measured at 15 °C, 30 °C, and 45 °C. In addition, only at 0 °C, the charge profiles exhibited short, plateau-like portions at around 4.50–4.55 V, formed continuously during charging to 4.7 V in the 2nd to 5th cycles. This continuously developed plateau-like portion of the charging process at 0 °C, though at lower potential compared to the plateau during the first charge (Figure 2a), seemed to be thermodynamically favorable and may have indicated a continuous activation of Li₂MnO₃ and the Li⁺ extraction from the structure. They were gradually progressing, in contrast to the voltage plateaus that developed only in the first charging process of Li₂MnO₃ electrodes at 30 °C and 45 °C, shown in Figure 2b,c. In addition, Figure S4, that shows differential capacity plots of the above Li₂MnO₃ electrode cycled at 0 °C, also exhibits dQ/dV peaks at potentials close to those of the voltage plateaus.

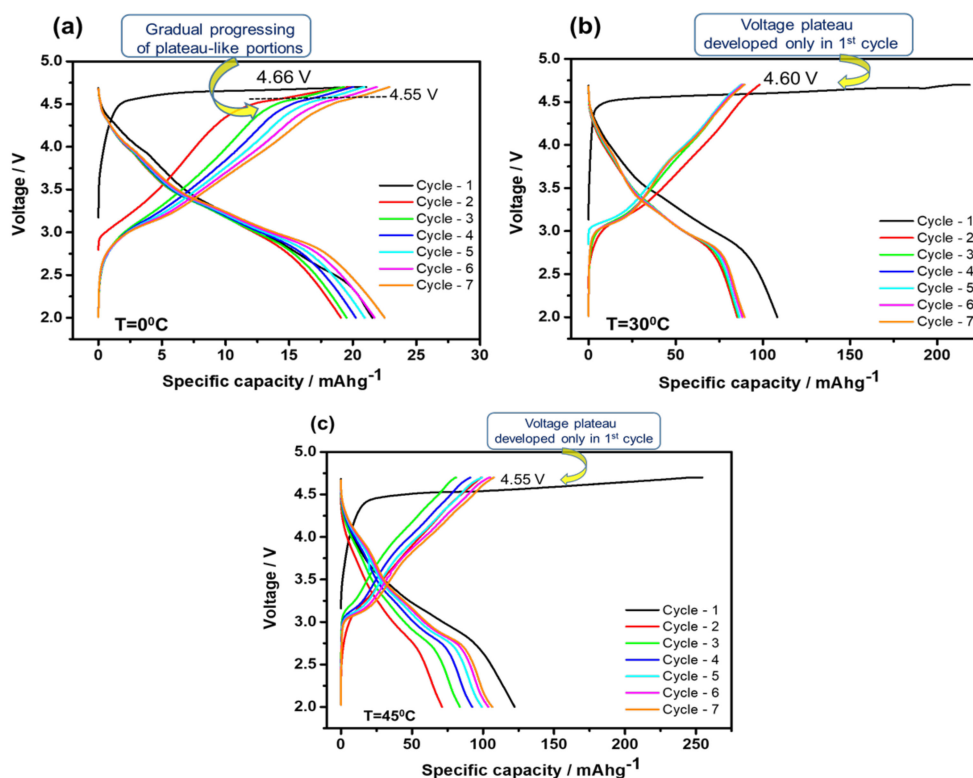
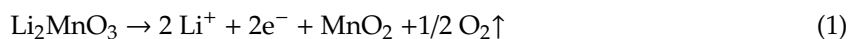


Figure 2. Voltage profiles of Li_2MnO_3 electrodes measured during several initial cycles at 0°C (a), 30°C (b), and 45°C (c). The current density applied was 2 mA/g . Potentials of the plateaus registered upon the charging of electrodes to 4.7 V are indicated. At the upper cut-off voltage of 4.7 V , electrodes were kept potentiostatically for 1 h . Note that at 0°C , plateau-like portions of the charging profiles registered at $\sim 4.55\text{ V}$ developed in a step-wise manner, as indicated in (a).

A similar continuous activation of Li_2MnO_3 reflected by gradually developed, plateau-like portions during charging to 4.8 V for the initial five cycles was also observed by Ye et al. [69] in Li-rich $\text{Li}[\text{Li}_{1/3-2x/3}\text{Mn}_{2/3-x/3}\text{Ni}_x]\text{O}_2$ ($0.09 \leq x \leq 0.2$) materials doped with minor amounts of nickel. These authors attributed the continuous or stepwise gradual activation of Li_2MnO_3 to smaller (optimized) amounts of dopant.

Figure 3a–c shows that the discharge capacities delivered in the initial cycles at 0°C and 45°C increased up to ~ 22 and 100 mAh/g , respectively, while those at 30°C were stabilized at around 90 mAh/g . We note that the relatively low capacities obtained at 30°C and 45°C from electrodes comprising Li_2MnO_3 submicronic (partially agglomerated) particles are in line with the values demonstrated in our previous work [58]. It should be noted that a high specific capacity ($>200\text{ mAh/g}$) can be extracted from Li_2MnO_3 electrodes only if the active mass comprises nanoparticles. The active mass used herein comprised too big particles, and therefore, the maximal specific capacity that could be demonstrated was 100 mAh/g . However, in this work, the focus is not the optimization of performance in terms of high capacity, but rather, understanding the effect of temperature on the activation process, which is very complicated. The complex process of the Li^+ -ion extraction above 4.5 V from Li- and Mn-rich electrodes (activation) reflected by the potential plateau involves the simultaneous extraction of oxygen from the lattice, and the rearrangement of Mn ions in the case of Li_2MnO_3 or TM ions (Mn, Ni, Co) in the case of $x\text{Li}_2\text{MnO}_3 \cdot (1-x)\text{Li(TM)}\text{O}_2$ materials. This process can be represented as follows [56,70]:



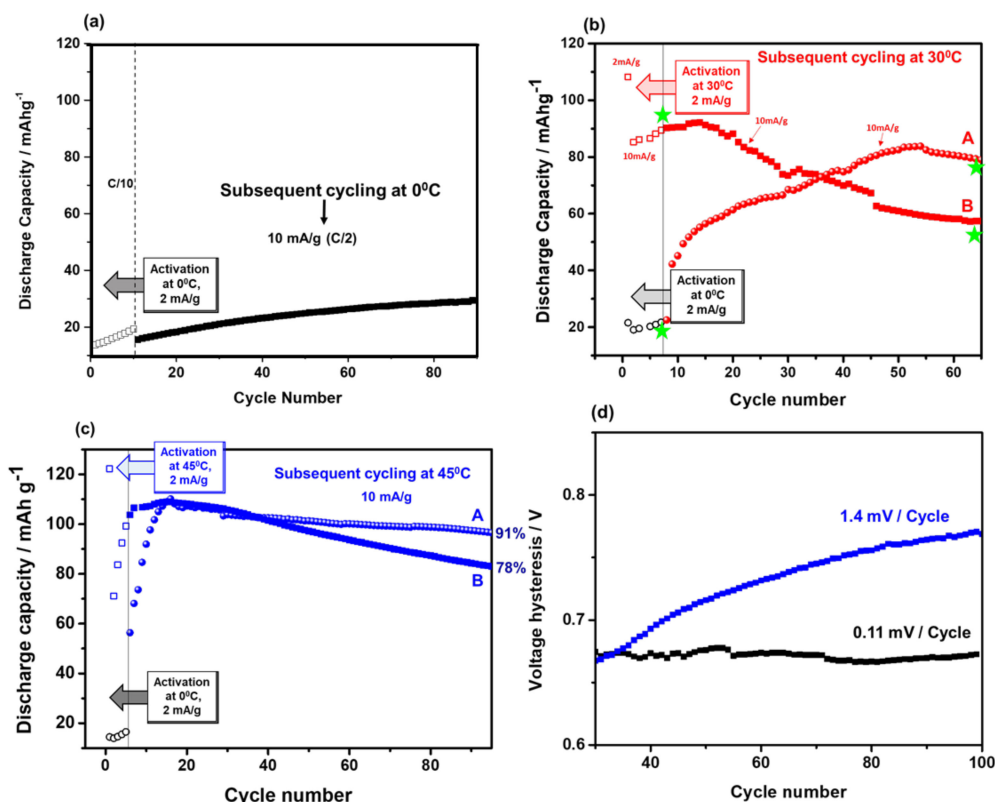
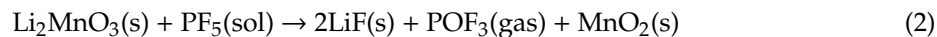


Figure 3. (a) Discharge capacity of Li_2MnO_3 electrodes activated at 0 °C for several initial cycles (empty symbols). Current density was 2 mA/g corresponded to $\sim C/10$ rate. Subsequent cycles (10 mA/g, $\sim C/2$ rate) at this temperature are also shown (filled symbols). (b) Left hand portion: discharge capacity of several initial activation cycles of Li_2MnO_3 electrodes at 0 °C (black symbols; 2 mA/g, $\sim C/10$) and at 30 °C (red symbols). In the right hand portion, curve A exhibits discharge capacity of Li_2MnO_3 electrodes activated at 0 °C and subsequently cycled at 30 °C (10 mA/g, $\sim C/2$). Curve B relates to the case when both activation and the subsequent cycling were performed at 30 °C. Note that in both cases of activation at 0 °C or at 30 °C, the subsequent cycling was performed at the same C/2 rate, for the direct comparison. Impedance spectra of Li_2MnO_3 electrodes were measured at 30 °C, at 4.4 V upon charging at points marked with green stars. Typical impedance spectra are shown in Figure S6. (c) Left hand portion: discharge capacity of several initial activation cycles of Li_2MnO_3 electrodes at 0 °C (black circles; 2 mA/g, $\sim C/10$) and 45 °C (blue squares). In the right hand portion, curve A exhibits discharge capacity of Li_2MnO_3 electrodes activated at 0 °C and subsequently cycled at 45 °C (10 mA/g, $\sim C/2$). Curve B relates to the case when both activation and the subsequent cycling were performed at 45 °C. Capacity retention (in %) of these electrodes calculated from 20th to 95th cycles is indicated. (d) Black curve displays the voltage hysteresis of Li_2MnO_3 electrodes activated at 0 °C for a few initial cycles and subsequently cycled at 45 °C. Blue curve: both activation and the subsequent cycling were performed at 45 °C, as demonstrated in Figure 3c. Changes of the voltage hysteresis per cycle are indicated.

Recent studies by the Gasteiger's group using OEMS and HR-TEM [6,70,71] provided strong evidence that oxygen is released not from the bulk Li_2MnO_3 , but irreversibly from a several nm thick near-surface layer of $x\text{Li}_2\text{MnO}_3 \cdot (1-x)\text{Li(TM)}\text{O}_2$ materials. It is important to emphasize that upon charging to high potentials, oxygen can be oxidized to per-oxo species ($2\text{O}^{2-} \leftrightarrow \text{O}_2^{2-} + 2e^-$) and then released as gaseous O_2 [45,72]. This reversible oxo- (O^{2-}) to per-oxo like (O_2) $^{n-}$ transformation upon charge/discharge of Li-rich oxides is driven by a reductive coupling mechanism, and is still under intensive study [73,74]. As follows from the results in Figure 3a–c, the maximal charge capacities obtained in the 1st cycle at 0 °C, 30 °C, and 45 °C were, respectively 27, 212, and 227 mA h g^{-1} . They correspond to ~ 6 , 46, and 49% of the Li-ions extracted from Li_2MnO_3 , taking into account its theoretical capacity of ~ 460 mA h g^{-1} for 2 Li^+ extracted per chemical formula. The corresponding discharge

capacities delivered in the 1st cycles at these temperatures were 21, 110 and 113 mAh/g, with calculated irreversible capacity losses (ICL) of 1.8, 51, and 52% respectively. The lowest ICL at 0 °C thus implies far fewer undesirable side reactions of the electrode material with traces of HF, PF₅ (strong Lewis acid) in EC-EMC/LiPF₆ solution, for instance:



This may also be related to the reduced interactions of the per-oxo like species formed and the oxygen released at 0 °C with the EC and EMC solvents. (O₂)ⁿ⁻ can promote reactions of the EC absorbed on the electrode surface and its decomposition (by breaking one of the two C–O bonds in the ring) that results in the evolution of CO₂ and other organic species [75]. Our suggestion on minor interfacial side reactions at 0 °C is consistent with the observed reduced oxygen activity upon charging at this temperature, compared to at 30 °C. This is demonstrated by the results of OEMS studies in Figure 4, and agrees well with the surface analysis of the oxygen XPS spectra of Li₂MnO₃ samples subjected to initial cycling at 0 °C and 30 °C (Figure 5).

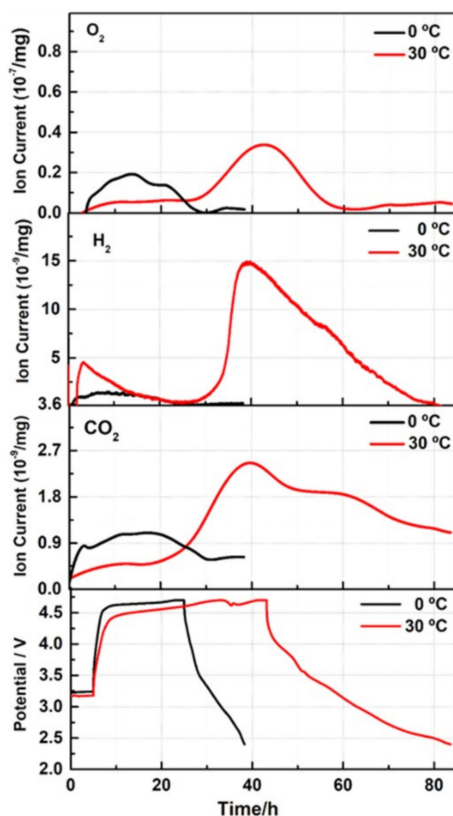


Figure 4. Evolution of gases O₂, H₂, and CO₂ with time during the 1st charge–discharge cycle of Li₂MnO₃ electrodes (shown in the bottom chart) measured by OEMS at 0 °C and 30 °C, as indicated. Since during 2nd to 7th initial cycles, less gas was evolved compared to the 1st one, the corresponding ion currents could not be adequately measured because of the instrumental limitations of OEMS. The upper cut-off voltage was 4.7 V in these experiments.

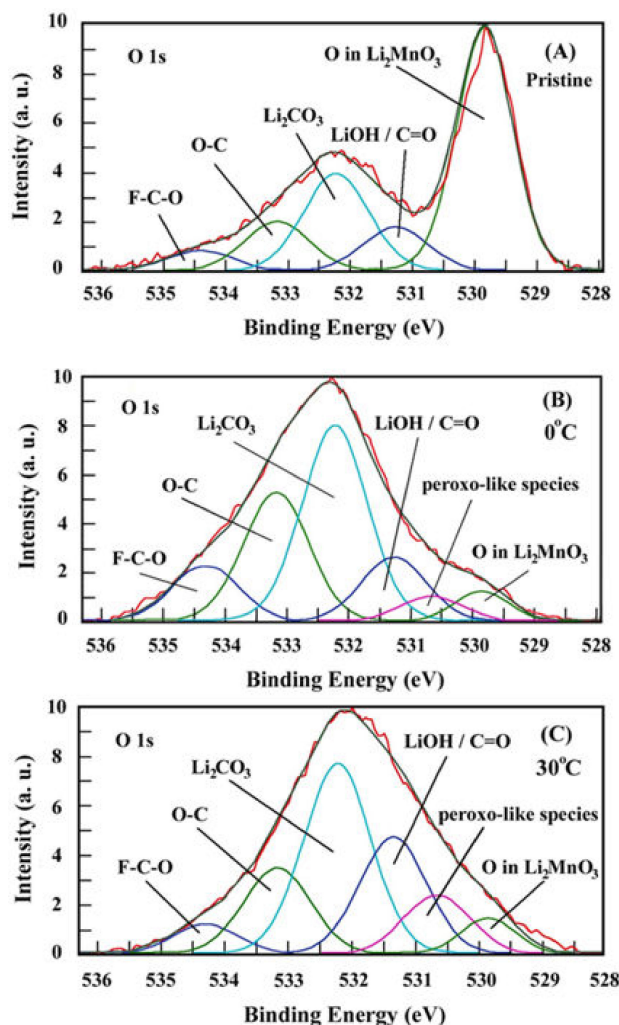


Figure 5. O1s XPS spectra measured from pristine (uncycled) Li_2MnO_3 electrode (A) and those subjected to the 1st charge–discharge cycles at 0°C and 30°C , (B) and (C), respectively. Voltage profiles of these electrodes are shown in Figure 2a,b.

From XPS measurements, we established that a lower amount (5.2%) of per-oxo like species is formed upon the 1st cycle of Li_2MnO_3 electrode at 0°C compared to that of 11.6% at 30°C ; see Figure 5 and Table S2. This is also evident from the comparative ratio of (lattice oxygen) to (per-oxo species), which was almost twice as high for the latter electrode. Note that the content of $(\text{O}_2)^{n-}$ species calculated from our high-resolution XPS studies agrees well with that number of 9% measured for discharged Li-rich $\text{Li}_{1.2}\text{Ni}_{0.13}\text{Mn}_{0.54}\text{Co}_{0.13}\text{O}_2$ materials presented in the work by Tarascon et al. [45]. We suggest that stabilized Li_2MnO_3 electrode/solution interface forms during the activation cycles at 0°C , compared to that at 30°C and 45°C , thus providing their stable subsequent cycling performance with higher capacity retention, as demonstrated in Figure 3b,c.

Clear evidence to support our suggestion comes in the form of the much lower charge-transfer resistance (R_{ct}) of Li_2MnO_3 electrodes initially activated at 0°C , compared to at 30°C , as demonstrated in Figure 6a. This represents the surface film (R_{sf}) and charge-transfer resistances of these electrodes as a function of the potential measured during the charging process up to 4.7 V. Figure 6b shows that after 65 cycles, R_{ct} also remained lower for electrodes activated at 0°C . Only at 4.6 V, R_{ct} increased, probably due to some structural disordering or rearrangements at the electrode surface at high anodic potentials. Note that information on resistances representing the electrochemical processes (as in Figure 6a,b) was obtained from the analysis of the data via Impedance Spectroscopy Genetic Programming. ISGP computes distribution function of relaxation times Γ in the form of Γ plotted vs.

$\log f$ (f is the frequency range from 100 kHz to 5 mHz used in impedance tests). These plots are shown in the Supplementary Materials Figure S5a–d.

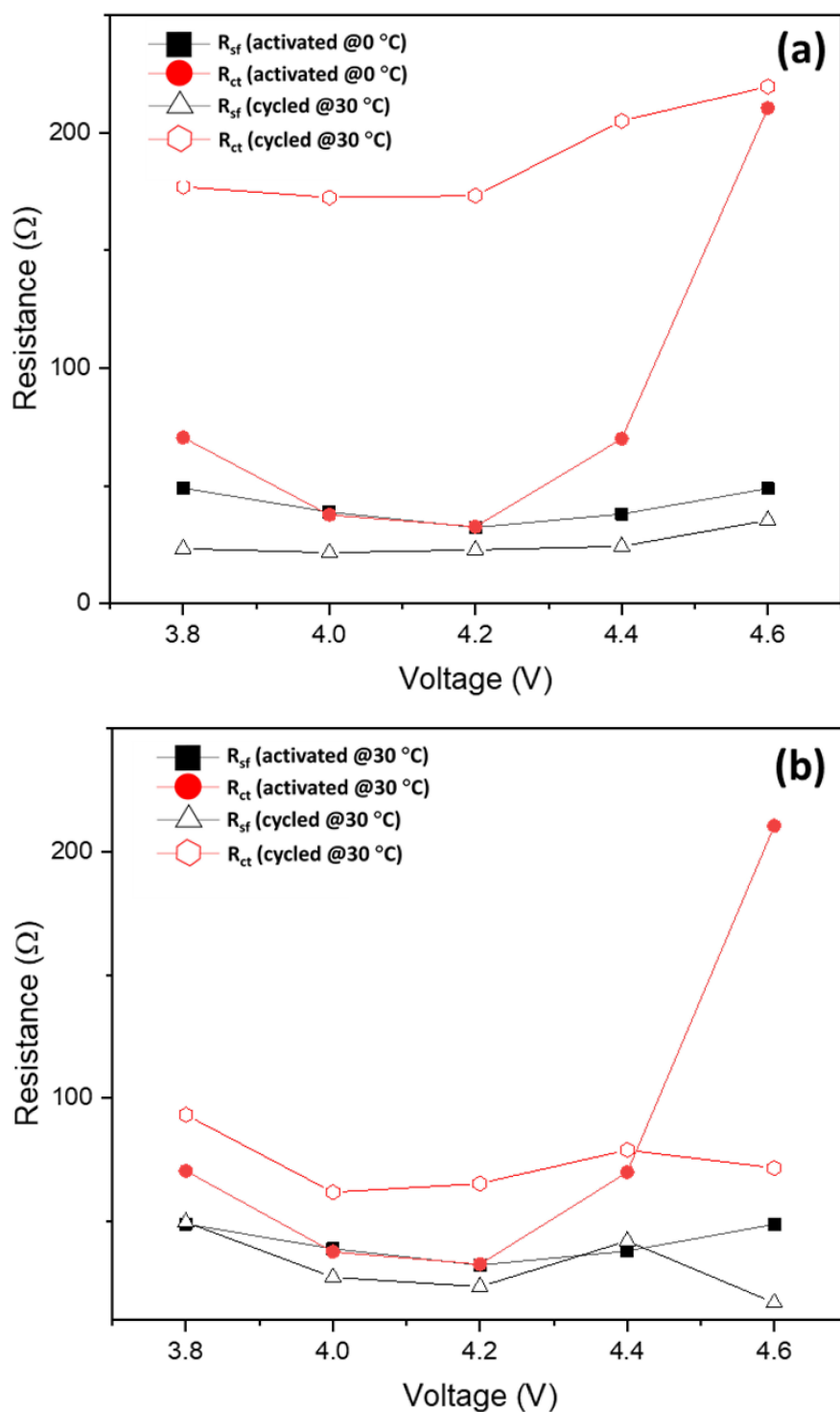


Figure 6. Surface film (R_{sf}) and charge-transfer (R_{ct}) resistances calculated from impedance spectra measured at 30 °C from Li_2MnO_3 electrodes initially activated at 0 °C (a) and 30 °C (b), respectively, as presented in Figure 3b, curves A and B. The corresponding points of impedance measurements are marked with green stars in Figure 3b. Typical impedance spectra (Nyquist plots) of these electrodes, measured at 30 °C at 4.4 V upon charging, are displayed in Figure S6.

The continuous “activation” of the Li_2MnO_3 phase at 0°C occurring upon charging to 4.7 V at potentials of 4.50–4.55 V was supported by the results of the galvanostatic intermittent titration technique (GITT) measurements, shown in Figure S7. These results confirm that only at 0°C during the 1st charging process of Li_2MnO_3 , the variation with time of the transient electrode potential exhibited short, plateau-like regions at 4.6 V, followed by an extended plateau, similar to that in Figure 2a. Thus, we consider the activation of Li_2MnO_3 electrodes at 0°C to be a step-by-step process that was not detected in the initial cycles at the higher temperatures of 30°C and 45°C . A few questions, therefore, can be addressed, like: What is the possible impact of this step-by-step activation during several initial cycles at 0°C on the subsequent electrode cycling at this temperature and at higher temperatures? What is its effect on the capacity fading, on the evolution of the voltage hysteresis and on electrode impedance? From the typical plot of the discharge capacity delivered by the Li_2MnO_3 electrode activated at 0°C and subsequently cycled at this temperature (Figure 3a), it is clearly seen that after the activation cycles, the capacity increases smoothly, reaching maximal values of $\sim 25\text{--}30\text{ mAh/g}$. In contrast, 3–4 times greater capacities can be obtained when Li_2MnO_3 is activated at 0°C and cycled at higher temperatures, i.e., 30°C or 45°C , as demonstrated by the cycling profiles (curves A) in Figure 3b,c, respectively. These results demonstrate that only when a few initial cycles were performed at a low temperature, providing step-by-step activation, the capacity increased substantially, and the capacity fading was less and the voltage hysteresis was considerably mitigated and stabilized upon cycling at a higher temperature (45°C), as demonstrated in Figure 3d. This is in line our previous findings [41], i.e., that the activation of Li- and Mn-rich cathodes ($0.35\text{Li}_2\text{MnO}_3\cdot 0.65\text{Li}[\text{Mn}_{0.45}\text{Ni}_{0.35}\text{Co}_{0.20}]\text{O}_2$) at low temperature results in an increased discharge capacity, decreased average charge voltage, and voltage hysteresis. As we noted in that paper, the results demonstrated by low temperature activation (“low-T activation”) of the above cathodes were similar to those shown by other groups using potential window opening or step-wise increasing anodic potential limits [15,45,76–78]. For instance, increased discharge capacity and decreased fading were observed by Sato et al. [78] and Ohsawa et al. [79], when cells with $\text{Li}[\text{Ni}_{0.17}\text{Li}_{0.2}\text{Co}_{0.07}\text{Mn}_{0.56}]\text{O}_2$ cathodes were cycled through step-wise precycling treatment, which included increasing the upper potential limit by 0.1 V from 4.5 V every two cycles to 4.8 V. This precycling treatment means reaching and traversing the voltage plateau several times, after which the Li-ions are extracted and the oxygen is released from the material. Dahn et al. [80] also came to a conclusion that a repeated stepwise traverse of the oxygen-release plateau resulted in higher cycling capacities of Li- and Mn-rich $\text{Li}[\text{Li}_{1/5}\text{Ni}_{1/5}\text{Mn}_{3/5}]\text{O}_2$ cathodes in Li-cells, compared to one-step oxygen release. By analyzing the literature data and the results obtained in the present work for Li_2MnO_3 electrodes activated at 0°C , we assume that this “low-T activation” indeed provided a useful repeated stepwise traversing of the voltage plateau at $>4.5\text{ V}$ over several cycles (from 2nd to 5th); see Figure 2a. These short, plateau-like portions were developed in a step-wise manner from the same cycling procedure upon charging Li_2MnO_3 to 4.7 V. The effect of the “low-T activation” was that the capacity of Li_2MnO_3 electrodes increased and leveled-off upon further cycling at 30°C , in contrast to those activated in one-step at 30°C and cycled at this temperature (Figure 3b, curves A and B, respectively). Stepwise activation at 0°C also pronouncedly affected the further cycling of Li_2MnO_3 at 45°C , resulting in a stabilized performance after “low-T activation”, as reflected by higher capacity retention and much lower and stabilized the voltage hysteresis; see Figure 3c,d, respectively. These findings are crucially important, since capacity fading and large voltage hysteresis are among the main problems which need to be resolved for Li- and Mn-rich cathode materials in advanced LIBs [2,4,5]. It is important to note that the effect of the “low-T activation” of Li_2MnO_3 discussed above confirms the hypothesized mechanism behind the improved electrochemical behavior of $0.35\text{Li}_2\text{MnO}_3\cdot 0.65\text{Li}[\text{Mn}_{0.45}\text{Ni}_{0.35}\text{Co}_{0.20}]\text{O}_2$ materials activated at 0°C in our earlier work [41]. This mechanism suggested a gradual, step-wise activation of these electrodes at 0°C , allowing slower structural activation/reorganization of the Li_2MnO_3 component to occur. This, in turn results in a greater degree of the TM-layer being accessible for Li^+ ion extraction/re-insertion and a smaller amount of the surface oxygen release. Indeed, as was confirmed by our OEMS and XPS studies of Li_2MnO_3 electrodes activated at 0°C , the amounts of O_2 evolved and per-oxo species formed

were lower compared to those at 30 °C (Figures 4 and 5, respectively). Below, we present the results of some structural studies of Li_2MnO_3 electrodes initially activated at 0 °C and 30 °C.

3.3. Structural Aspects of the Initial Cycling of Li_2MnO_3 Electrodes at 0 °C and 30 °C

It is evident from the voltage profiles of Li_2MnO_3 electrodes initially cycled at 0 °C, 30 °C, and 45 °C (Figure 2a–c) that electrochemical activities were developed at around 3 V. We propose that these electrochemical processes reflect the formation of spinel or spinel-like phases as a result of the layered-to-spinel transformation which is typical for Li(TM)O_2 cathode materials during charge–discharge cycling [28,35,49]. Figure 7 compares the XRD patterns of an uncycled (pristine) Li_2MnO_3 electrode with those of structurally identical electrodes initially charged to 4.7 V and discharged at 2.0 V at 0 °C and 30 °C, respectively.

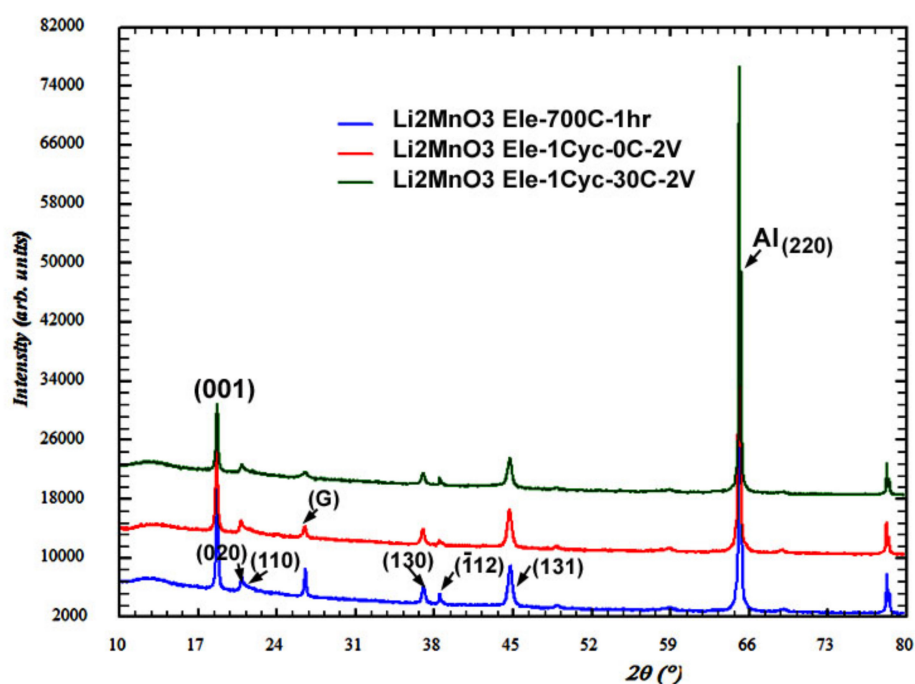


Figure 7. Comparison of XRD patterns recorded from Li_2MnO_3 electrodes on the Al-foil current collectors. Label G is related to a graphite peak, the peak at $2\theta = 65.1^\circ$ is associated with (220) reflection from Al-foil. Blue, red and green profiles correspond, respectively, to as-prepared (annealed) powder and to electrodes subjected to the first charge–discharge cycle at 0 °C and 30 °C.

As follows from Table S1, the unit cell parameters of cycled Li_2MnO_3 only slightly changed compared to those of the pristine electrode. The XRD patterns recorded from the cycled electrodes did not show any new peaks in addition to the peaks of the monoclinic phase. Nevertheless, the TEM examinations revealed that the tetragonal spinel $\text{Li}_2\text{Mn}_2\text{O}_4$, described by space group $I4amd$ [81], was formed in electrodes even during the first cycle, both at 0 °C and at 30 °C. The cell parameters of $\text{Li}_2\text{Mn}_2\text{O}_4$ were calculated as follows: $a = 17.540 \text{ \AA}$ and $c = 8.205 \text{ \AA}$. The corresponding TEM micrographs taken from samples subjected to the first cycle at 0 °C and at 30 °C are shown, respectively, in Figure 8a,b. The inserts in these figures represent the convergent-beam electron diffraction (CBED) patterns, which were taken from the grains indicated by arrows. The bottom inserts correspond to the main monoclinic Li_2MnO_3 phase, and the upper inserts contain patterns indexed in terms of the tetragonal spinel $\text{Li}_2\text{Mn}_2\text{O}_4$. The upper insert in Figure 8b also contains an additional reflection system associated with the monoclinic phase (m). The high-resolution image in Figure S8 is an additional illustration of the presence of tetragonal spinels in the Li_2MnO_3 electrode after the first charge–discharge cycle. This image was taken from a grain related to the upper insert

in Figure 8a. As expected, the corresponding Fourier transformed electron diffraction data were indexed to the tetragonal spinel $\text{Li}_2\text{Mn}_2\text{O}_4$ in full accordance with the CBED pattern recorded from this grain.

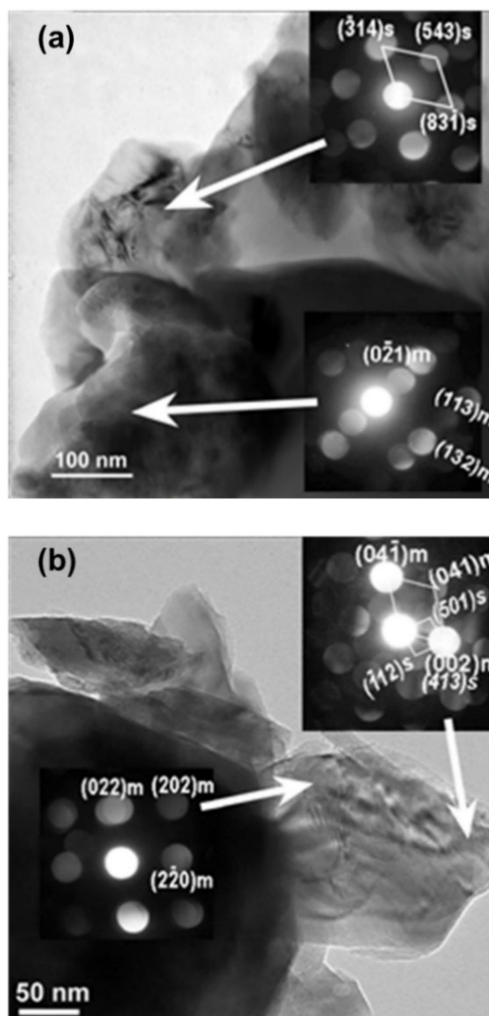


Figure 8. (a) TEM micrograph of Li_2MnO_3 electrode after the first charge/discharge cycle at 0 °C. The inserts show CBED patterns, which were taken from grains indicated by arrows. The pattern in the bottom insert is indexed on the basis of the monoclinic Li_2MnO_3 phase (m), and the pattern in the upper insert demonstrates the presence of the tetragonal spinel $\text{Li}_2\text{Mn}_2\text{O}_4$ (s). (b) TEM micrograph of Li_2MnO_3 electrode after the first charge/discharge cycle at 30 °C. The inserts show CBED patterns taken from grains indicated by arrows. The bottom pattern is indexed to the monoclinic Li_2MnO_3 phase (labeled m), and the pattern in the upper insert contains two systems of reflections related to the monoclinic phase (m) and to the tetragonal spinel (s).

The results of the electron-diffraction studies demonstrating the formation of the spinel phase after the first cycle were supported by Raman spectroscopy measurements. Figure 9 exhibits a typical Raman spectrum of a pristine Li_2MnO_3 (uncycled) electrode, showing several well-resolved peaks (bands) at 603, 560, 428, 409, 369, 305, and 246 cm^{-1} . These are in agreement with the literature reports on the monoclinic Li_2MnO_3 phase [67]. However, the Raman responses of electrodes subjected to a first cycle show some changes, namely a decreased intensity of the main peak at 603 cm^{-1} , its asymmetry and broadening related to a cationic disorder, and increasing the amount of stacking faults [82].

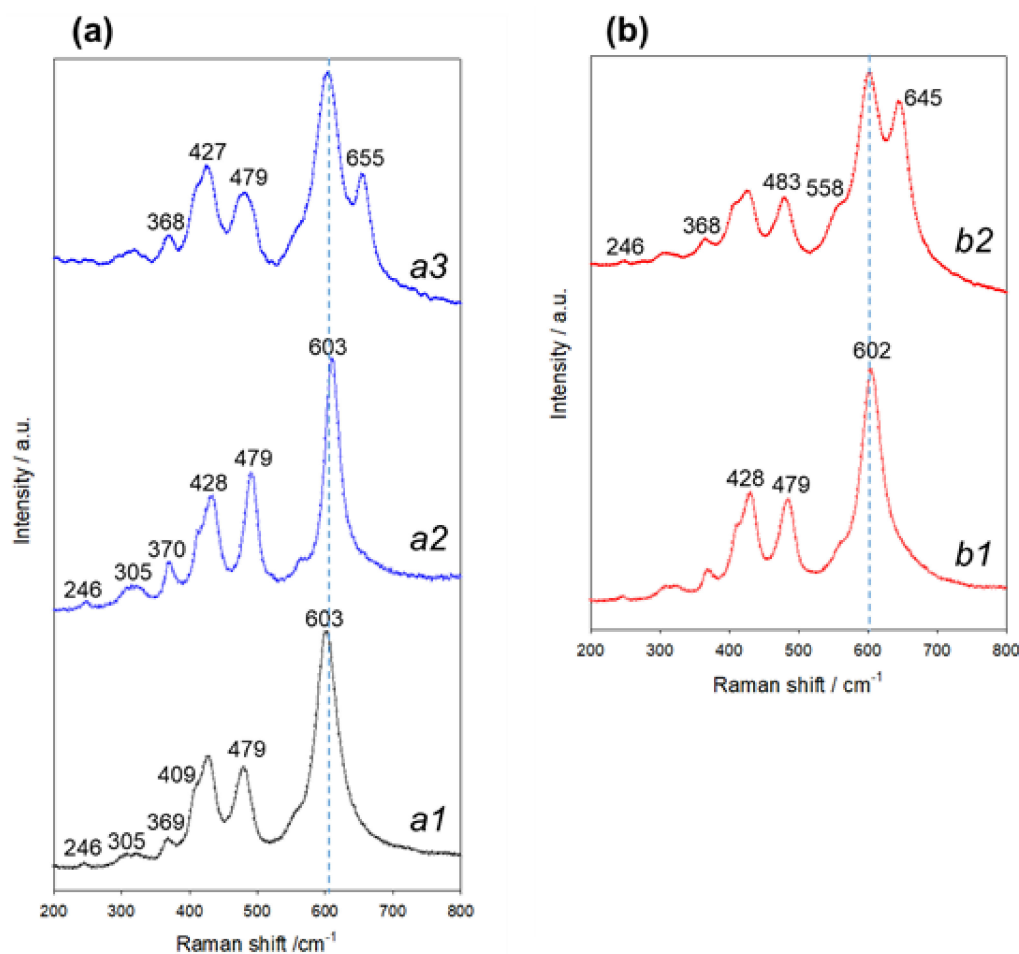
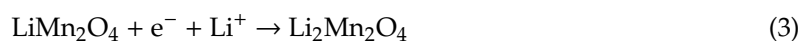


Figure 9. (a) Typical Raman spectra of pristine (uncycled) Li₂MnO₃ electrode (*a1*) and of a similar electrode after the 1st charge–discharge cycle at 0 °C measured at arbitrary locations (*a2*) and (*a3*); (b) spectra related to Li₂MnO₃ electrode after the 1st charge–discharge cycle at 30 °C measured at arbitrary locations (*b1*) and (*b2*).

We suggest that at anodic potentials >4.5 V, the Li⁺-ions can be further extracted from the LiMn₂O₄ phase formed due to the layered-to-spinel transition (as demonstrated by electron diffraction studies, Figure 8a,b), providing emerging of new Raman bands at wavenumbers ~655 and 645 cm⁻¹ in the spectra of Li₂MnO₃ electrodes cycled at 0 °C and 30 °C, respectively [83]. Upon the discharging process, Li⁺ ions can be inserted into the cubic spinel species to form the tetragonal phase according to the following reaction:



An important piece of information on structural bulk and surface changes of Li₂MnO₃ electrodes subjected to initial charge–discharge cycles at 0 °C and 30 °C was obtained from Extended X-ray Absorption Fine Structure–X-ray Absorption Near Edge Structure (EXAFS–XANES) and high-resolution XPS studies. As seen in Figure 10a, the XANES data of the Li₂MnO₃ electrode cycled at 0 °C were almost identical to those of the as-prepared pristine material, which indicates the same oxidation state of Mn in these samples. Note that along with Mn⁴⁺, some Mn³⁺ ions may also be present in the disordered surface layer of Li₂MnO₃ electrodes subjected to charge–discharge cycle. This is in accordance with an analysis of the magnetic characteristics of these electrodes at various states-of-charge, as discussed in [84]. In addition, one should take into account that Mn³⁺-containing species (LiMnO₂) can be formed upon oxygen release from the surface of Li₂MnO₃. Moreover, as shown in a recent work [85], based on the calculation of Bader charges and magnetic moments, the Mn oxidation state in HE-NCM

can be reduced in the presence of per-oxo like $(O_2)^{2-}$ as a result of anionic charge overcompensation. The EXAFS data of Li_2MnO_3 cycled at $0\text{ }^\circ\text{C}$ and $30\text{ }^\circ\text{C}$ (Figure 10b,c, respectively) have similar features to the pristine Li_2MnO_3 . The major change in the electrode cycled at $30\text{ }^\circ\text{C}$ was observed as the reduced amplitude in the EXAFS data, probably because of the structural disorder near the Mn sites. From the fitting results (Table S3 and Figure S9) of the EXAFS data, we conclude that an increase occurred in the obtained Debye-Waller factors for Mn-O1 and Mn-Mn paths in the Li_2MnO_3 sample cycled at $30\text{ }^\circ\text{C}$, compared with the as-prepared material and the cathode material cycled at $0\text{ }^\circ\text{C}$. Such changes in the Debye-Waller factors were very likely due to structural disorder near the Mn sites, which may be the main reason for the reduction of the amplitude of Mn-O1 and Mn-Mn peaks in the Li_2MnO_3 electrode after charge–discharge at $30\text{ }^\circ\text{C}$.

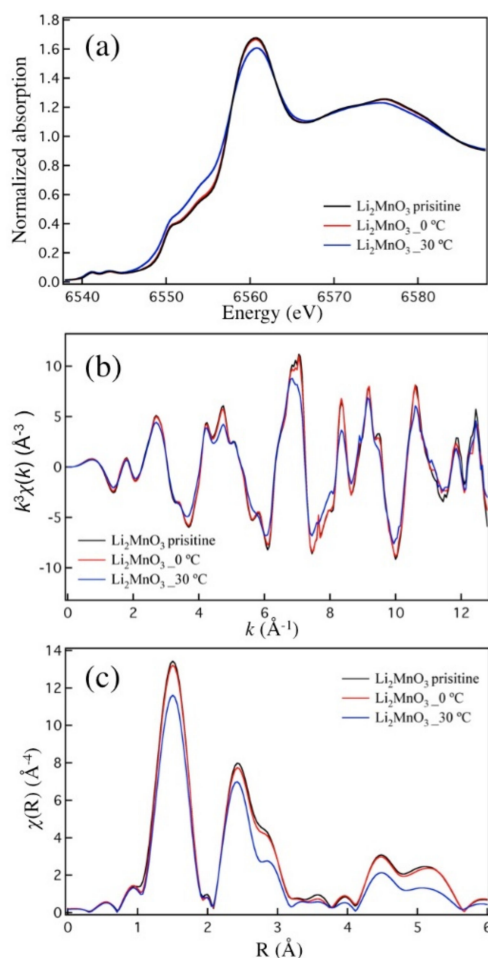


Figure 10. (a) Normalized Mn K-edge XANES spectra of Li_2MnO_3 samples: pristine powder and electrodes after the 1st cycle (charge to 4.7 V, discharge to 2.0 V) at $0\text{ }^\circ\text{C}$ and $30\text{ }^\circ\text{C}$, as indicated. The voltage profiles of these electrodes are shown in Figure 2a,b, respectively. (b) k^3 -weighted EXAFS $\chi(k)$ of Li_2MnO_3 samples: pristine powder and electrodes after the 1st cycle (charge to 4.7 V, discharge to 2.0 V) at $0\text{ }^\circ\text{C}$ and $30\text{ }^\circ\text{C}$, as indicated. The voltage profiles of these electrodes are shown in Figure 2a,b, respectively. (c) Fourier Transform magnitude of k^3 -weighted EXAFS data ($|\chi(R)|$) of Li_2MnO_3 samples (k -range: $2.5\text{--}11\text{ \AA}^{-1}$; R_{bkg} : 1.25 \AA).

High-resolution XPS data of the above samples also demonstrate that in Li_2MnO_3 electrodes subjected to initial cycling at $0\text{ }^\circ\text{C}$ and $30\text{ }^\circ\text{C}$, some surface species are formed with the Mn-oxidation states both of 3+ and 2+. This is evident from comparing the XPS spectra of manganese. The Mn 2p structure of cycled samples (Figure S10a) was slightly shifted to lower energy and highly broadened at its lower-energy side, raising the possibility of the formation of additional phases with Mn valences

lower than 4+ in pristine (uncycled) Li_2MnO_3 . This was indeed confirmed by the measured Mn 3s structure, that demonstrated a peak splitting (Δ , eV) higher than that of Li_2MnO_3 , as illustrated in Figure S10b. For the pristine sample $\Delta \sim 4.50$ eV, in contrast to initially cycled Li_2MnO_3 at 0 °C and 30 °C, the peak splitting values were estimated from XPS spectra as $\Delta \sim 5.60$ and $\Delta \sim 6.30$ eV, respectively corresponding to the Mn^{3+} and Mn^{2+} species formed on the surface of the Li_2MnO_3 particles [86].

4. Conclusions

We established in this work that initial (activation) cycling of Li_2MnO_3 electrodes performed at 0 °C results in increased discharge capacity, higher capacity retention, and decreased and stabilized voltage hysteresis upon subsequent cycling at higher temperatures, i.e., 30 °C or 45 °C. This is due to the fact that at 0 °C, Li_2MnO_3 electrodes undergo step-by-step activation, providing stepwise traversing of the voltage plateau at >4.5 V over several initial cycles. Importantly, activation cycling performed at 30 °C or 45 °C is characterized by voltage plateaus at 4.60 and 4.55 V, respectively, that develop only in the first charging process of Li_2MnO_3 electrodes; in contrast to 0 °C activation, this leads to considerable capacity fading and substantially increased voltage hysteresis in further cycling. These findings are in accordance with those reported by us previously [41]: The activation of $0.35\text{Li}_2\text{MnO}_3 \cdot 0.65\text{Li}[\text{Mn}_{0.45}\text{Ni}_{0.35}\text{Co}_{0.20}]\text{O}_2$ materials comprising Li_2MnO_3 as the main component at 0 °C leads to extra capacity of these electrodes. This results in an increased discharge capacity, decreased average charge voltage, and lower voltage hysteresis. We conclude that the irreversible capacity loss of Li_2MnO_3 electrodes activated at 0 °C is relatively low. The amount of per-oxo like species formed and the oxygen, H_2 , and CO_2 released during activation at low temperature were also lower compared to cathodes activated at 30 °C and 45 °C. This indicates the occurrence of fewer interfacial side reactions and the formation of an improved surface passivation at 0 °C. The considerably lower charge-transfer resistance of these electrodes, calculated from impedance spectra measured upon charging to 4.7 V, also supports this conclusion. We furthermore conclude that Li_2MnO_3 preserved its bulk structure upon activation cycles at 0 °C and 30 °C, with only some structural disorder near the Mn-sites (at 30 °C) and partial transformation (at the particle surface) from the layered-type ordering to a tetragonal spinel $\text{Li}_2\text{Mn}_2\text{O}_4$ phase, which is typical for these systems.

We believe that the present work on initial (activation) cycling of Li_2MnO_3 at 0 °C resulting in improved behavior when continuing operation at higher temperature is important for understanding the complex activation mechanism of high specific capacity Li- and Mn-rich NCM cathode materials for advanced Li-ion batteries.

Supplementary Materials: The following are available online at <http://www.mdpi.com/1996-1944/13/19/4388/s1>. Figure S1: Scanning Electron Microscopy image of the as-prepared Li_2MnO_3 annealed consequently at 400° and 700 °C for 1 h at each temperature, under air. Figure S2: XRD pattern collected from the as-prepared Li_2MnO_3 powder, which was annealed consequently at 400° and 700 °C for 1 h at each temperature, under air. Figure S3: High-resolution image taken from the particle indicated by the arrow in Figure 1. The distances between the atomic planes of 0.43 nm and 0.41 nm match, respectively, the interplanar spacings d_{020} , and d_{110} in the monoclinic Li_2MnO_3 structure. The Fourier transform in the insert looks exactly the same as the CBED pattern in the insert in Figure 1. Figure S4: Differential capacity dQ/dV profiles of Li_2MnO_3 electrodes measured during several initial cycles at 0 °C (a), 30 °C (b), and 45 °C (c) as shown in Figure 3. Figure S5: The DFRT for impedance of Li_2MnO_3 electrodes measured at 30 °C after initial activation cycles performed at 0 °C (a) and after subsequent cycling at 30 °C (b), and for similar Li_2MnO_3 electrodes measured at 30 °C after initial activation cycles performed at 30 °C (c) and after subsequent cycling at the same temperature of 30 °C (d) Peaks correspond to surface film (sf) and charge-transfer (ct) resistances. Typical impedance spectra of Li_2MnO_3 electrodes measured at 30 °C at 4.4 V upon charging are shown in Figure S6. Typical impedance spectra (Nyquist plots) of Li_2MnO_3 electrodes measured at 4.4 V upon charging, at 30 °C. Four points of impedance measurements are marked with green stars in Figure 3b, namely: (a) after activation cycles at 0 °C; (b) after activation cycles at 0 °C with subsequent cycling at 30 °C; (c) after activation cycles at 30 °C; (d) after activation cycles at 30 °C with subsequent cycling at 30 °C. Figure S7 Variations with time of the transient electrode potential measured during the 1st charging process by three subsequent GITT titration stages of Li_2MnO_3 samples at 0 °C (a) and 30 °C (b). Coin-type cells, LP-57 solution. The current density applied was $\sim 4 \mu\text{A}/\text{cm}^2$ corresponding to $\sim 2 \text{ mA}/\text{g}$. Semi-filled, filled, and empty symbols relate to OCV potentials of 4.10 V, 4.36 V, and 4.42 V in (a) and 4.33 V, 4.35 V, and 4.36 V in (b), respectively. Figure S8. High-resolution image taken from the particle shown in Figure 7a. This particle was identified as the tetragonal spinel $\text{Li}_2\text{Mn}_2\text{O}_4$. The indexed Fourier transform shown in the insert is in accordance with the corresponding

CBED pattern in Figure 7a. Figure S9. Mn K-edge Fourier transform magnitudes of k^3 -weighted EXAFS data and theoretical fits of Li_2MnO_3 materials: pristine powder (a) and electrodes after the 1st cycle at 0 °C (b) and at 30 °C (c). Figure S10. Mn 2p and Mn 3s XPS spectra, (a) and (b), respectively measured from uncycled (pristine) Li_2MnO_3 electrode (red lines) and those subjected to the first charge-discharge cycles at 0 °C and 30 °C (green and blue lines, respectively). The Mn 3s spectra include color-coded values for the magnitude of the splitting Δ , eV between the two peaks. Voltage profiles of these Li_2MnO_3 electrodes are shown in Figure 2a,b. Table S1. Cell parameters of Li_2MnO_3 materials calculated from the corresponding XRD patterns. Table S2. Results of XPS measurements of the lattice oxygen in Li_2MnO_3 , per-oxo like and other components as calculated by fitting of the corresponding O 1s spectra measured from pristine (uncycled) Li_2MnO_3 electrode and those after initial activation cycles at 0° and 30 °C. The corresponding binding energies (in eV) are shown in blue color. Table S3. Best fit results for the structural parameters obtained by analysis of the Mn K-edge EXAFS data of Li_2MnO_3 samples: pristine powder and electrodes after the 1st cycle (charge to 4.7 V, discharge to 2.0 V) at 0° and 30 °C. N: coordination number; R: interatomic distance; σ^2 : Debye-Waller factor (mean-square disorder in R); ΔE_0 : Energy shift; (amp): the amplitude reduction factor.

Author Contributions: Conceptualization, B.M. and F.A.S.; methodology, E.E., B.M., F.A.S., A.I.F., J.L.; validation, F.A.S., M.T., L.B., A.I.F., J.L., R.; formal analysis, T.P., Y.T., R., M.N.; investigation, F.A.S., A.I.F., J.L., R.; data curation, B.M., M.T., A.I.F.; writing—original draft preparation, M.T., A.I.F., Y.G., B.M.; writing—review and editing, B.M., D.A., Y.T.; visualization, J.L., M.T., T.P.; supervision, D.A.; project administration, D.A. All authors have read and agreed to the published version of the manuscript.

Funding: A.I.F. was funded by the U. S. National Science Foundation Grant number DMR-1911592. BL2-2 beamline operations were supported in part by the Synchrotron Catalysis Consortium (U.S. DOE, Office of Basic Energy Sciences, Grant No. DE-SC0012335).

Acknowledgments: A part of the work discussed herein was supported by the Israeli Prime Minister's Office and by the Israeli Committee for Higher Education within the framework of the INREP project. B.M. and F.A.S. thank Daniela Kovacheva from Bulgarian Academy of Science for her helpful suggestions on the synthesis of Li_2MnO_3 and Ronen Y. Tirrer from Electronics Unit, Bar-Ilan University for technical support and valuable suggestions.

Conflicts of Interest: The authors declare no conflict of interest.

References

1. Thackeray, M.M.; Johnson, C.S.; Vaughey, J.T.; Li, N.; Hackney, S.A. Advances in manganese-oxide 'composite' electrodes for lithium-ion batteries. *J. Mater. Chem.* **2005**, *15*, 2257–2267. [[CrossRef](#)]
2. Nayak, P.K.; Erickson, E.M.; Schipper, F.; Penki, T.R.; Munichandraiah, N.; Adelhelm, P.; Sclar, H.; Amalraj, F.; Markovsky, B.; Aurbach, D. Review on challenges and recent advances in the electrochemical performance of high capacity Li and Mn-rich cathode materials for Li-Ion batteries. *Adv. Energy Mater.* **2018**, *8*, 1702397. [[CrossRef](#)]
3. Amalraj, F.; Talianker, M.; Markovsky, B.; Sharon, D.; Burlaka, L.; Shafir, G.; Zinigrad, E.; Haik, O.; Aurbach, D.; Lampert, J.; et al. Study of the lithium-rich integrated compound $x\text{Li}_2\text{MnO}_3 \cdot (1-x)\text{LiMO}_2$ (x around 0.5; $M = \text{Mn, Ni, Co}$; 2:2:1) and its electrochemical activity as positive electrode in lithium cells. *J. Electrochem. Soc.* **2013**, *160*, A324–A337. [[CrossRef](#)]
4. Erickson, E.M.; Schipper, F.; Penki, T.R.; Shin, J.-Y.; Erk, C.; Chesneau, F.-F.; Markovsky, B.; Aurbach, D. Review—Recent advances and remaining challenges for lithium ion battery cathodes. *J. Electrochem. Soc.* **2017**, *164*, A6341–A6348. [[CrossRef](#)]
5. Zheng, J.; Myeong, S.; Cho, W.; Yan, P.; Xiao, J.; Wang, C.; Cho, J.; Zhang, J. Li- and Mn-rich cathode materials: Challenges to commercialization. *Adv. Energy Mater.* **2017**, *7*, 1601284. [[CrossRef](#)]
6. Kleiner, K.; Strehle, B.; Baker, A.R.; Day, S.J.; Tang, C.C.; Buchberger, I.; Chesneau, F.-F.; Gasteiger, H.A.; Piana, M. Origin of high capacity and poor cycling stability of Li-rich layered oxides: A long-duration in situ synchrotron powder diffraction study. *Chem. Mater.* **2018**, *30*, 3656–3667. [[CrossRef](#)]
7. Jung, R.; Metzger, M.; Maglia, F.; Stinner, C.; Gasteiger, H.A. Oxygen release and its effect on the cycling stability of $\text{LiNi}_x\text{Mn}_y\text{Co}_z\text{O}_2$ (NMC) cathode materials for Li-Ion batteries. *J. Electrochem. Soc.* **2017**, *164*, A1361–A1377. [[CrossRef](#)]
8. Zhang, X.; Wei, Z.; Dinh, K.N.; Chen, N.; Chen, G.; Du, F.; Yan, Q. Layered oxide cathode for potassium-Ion battery: Recent progress and prospective. *Small* **2020**, 2002700. [[CrossRef](#)]
9. Zhao, C.; Lu, Y.; Chen, L.; Hu, Y. Flexible Na batteries. *InfoMat* **2020**, *2*, 126–138. [[CrossRef](#)]
10. Hwang, J.-Y.; Myung, S.-T.; Sun, Y.-K. Recent progress in rechargeable potassium batteries. *Adv. Funct. Mater.* **2018**, *28*, 1802938. [[CrossRef](#)]

11. Yan, G.; Mariyappan, S.; Rouse, G.; Jacquet, Q.; Deschamps, M.; David, R.; Mirvaux, B.; Freeland, J.W.; Tarascon, J.-M. Higher energy and safer sodium ion batteries via an electrochemically made disordered $\text{Na}_3\text{V}_2(\text{PO}_4)_2\text{F}_3$ material. *Nat. Commun.* **2019**, *10*, 1–12. [[CrossRef](#)]
12. Tanibata, N.; Kondo, Y.; Yamada, S.; Maeda, M.; Takeda, H.; Nakayama, M.; Asaka, T.; Kitajou, A.; Okada, S. Nanotube-structured $\text{Na}_2\text{V}_3\text{O}_7$ as a cathode material for sodium-ion batteries with high-rate and stable cycle performances. *Sci. Rep.* **2018**, *8*, 1–7. [[CrossRef](#)] [[PubMed](#)]
13. Gao, X.; Wang, D.; Lian, R.; Kan, D.; Mamoor, M.; Wang, C.; Chen, G.; Gao, C.; Wei, Y. Electronic properties, phase transformation and anionic redox of monoclinic Na_2MnO_3 cathode material for sodium-ion batteries: First-principle calculations. *ChemElectroChem* **2019**, *6*, 3987–3993. [[CrossRef](#)]
14. Hosaka, T.; Kubota, K.; Hameed, A.S.; Komaba, S. Research development on K-Ion batteries. *Chem. Rev.* **2020**, *120*, 6358–6466. [[CrossRef](#)] [[PubMed](#)]
15. Croy, J.R.; Gallagher, K.G.; Balasubramanian, M.; Long, B.R.; Thackeray, M.M. Quantifying hysteresis and voltage fade in $x\text{Li}_2\text{MnO}_3 \bullet (1-x)\text{LiMn}_{0.5}\text{Ni}_{0.5}\text{O}_2$ electrodes as a function of Li_2MnO_3 content. *J. Electrochem. Soc.* **2014**, *161*, A318–A325. [[CrossRef](#)]
16. Sathiya, M.; Abakumov, A.M.; Foix, D.; Rouse, G.; Ramesha, K.; Saubanère, M.; Doublet, M.L.; Vezin, H.; Laisa, C.P.; Prakash, A.S.; et al. Origin of voltage decay in high-capacity layered oxide electrodes. *Nat. Mater.* **2015**, *14*, 230–238. [[CrossRef](#)] [[PubMed](#)]
17. Hu, E.; Lyu, Y.; Xin, H.L.; Liu, J.; Han, L.; Bak, S.-M.; Bai, J.; Yu, X.; Li, H.; Yang, X.-Q. Explore the effects of microstructural defects on voltage fade of Li- and Mn-rich cathodes. *Nano Lett.* **2016**, *16*, 5999–6007. [[CrossRef](#)] [[PubMed](#)]
18. Croy, J.R.; Kim, D.; Balasubramanian, M.; Gallagher, K.; Kang, S.-H.; Thackeray, M.M. Countering the voltage decay in high capacity $x\text{Li}_2\text{MnO}_3 \bullet (1-x)\text{LiMO}_2$ electrodes (M = Mn, Ni, Co) for Li^+ -ion batteries. *J. Electrochem. Soc.* **2012**, *159*, A781–A790. [[CrossRef](#)]
19. Yu, X.; Lyu, Y.; Gu, L.; Wu, H.; Bak, S.-M.; Zhou, Y.; Amine, K.; Ehrlich, S.N.; Li, H.; Nam, K.-W.; et al. Understanding the rate capability of high-energy-density Li-rich layered $\text{Li}_{1.2}\text{Ni}_{0.15}\text{Co}_{0.1}\text{Mn}_{0.55}\text{O}_2$ cathode materials. *Adv. Energy Mater.* **2014**, *4*, 1300950. [[CrossRef](#)]
20. Lin, F.; Markus, I.M.; Nordlund, D.; Weng, T.-C.; Asta, M.D.; Xin, H.L.; Doeff, M.M. Surface reconstruction and chemical evolution of stoichiometric layered cathode materials for lithium-ion batteries. *Nat. Commun.* **2014**, *5*, 3529. [[CrossRef](#)]
21. Gent, W.E.; Lim, K.; Liang, Y.; Li, Q.; Barnes, T.; Ahn, S.-J.; Stone, K.H.; McIntire, M.; Hong, J.; Song, J.H.; et al. Coupling between oxygen redox and cation migration explains unusual electrochemistry in lithium-rich layered oxides. *Nat. Commun.* **2017**, *8*, 2091. [[CrossRef](#)] [[PubMed](#)]
22. Hu, E.; Yu, X.; Lin, R.; Bi, X.; Lu, J.; Bak, S.; Nam, K.-W.; Xin, H.L.; Jaye, C.; Fischer, D.A.; et al. Evolution of redox couples in Li- and Mn-rich cathode materials and mitigation of voltage fade by reducing oxygen release. *Nat. Energy* **2018**, *3*, 690–698. [[CrossRef](#)]
23. Hy, S.; Felix, F.; Rick, J.; Su, W.-N.; Hwang, B.J. Direct In situ observation of Li_2O evolution on Li-rich high-capacity cathode material, $\text{Li}[\text{Ni}_x\text{Li}_{(1-2x)/3}\text{Mn}_{(2-x)/3}]\text{O}_2$ ($0 \leq x \leq 0.5$). *J. Am. Chem. Soc.* **2014**, *136*, 999–1007. [[CrossRef](#)] [[PubMed](#)]
24. Xu, X.; Huo, H.; Jian, J.; Wang, L.; Zhu, H.; Xu, S.; He, X.; Yin, G.; Du, C.; Sun, X. Radially oriented single-crystal primary nanosheets enable ultrahigh rate and cycling properties of $\text{LiNi}_{0.8}\text{Co}_{0.1}\text{Mn}_{0.1}\text{O}_2$ cathode material for lithium-ion batteries. *Adv. Energy Mater.* **2019**, *9*, 1–9.
25. Singer, A.; Zhang, M.; Hy, S.; Cela, D.; Fang, C.; Wynn, T.A.; Qiu, B.; Xia, Y.; Liu, Z.; Ulvestad, A.; et al. Nucleation of dislocations and their dynamics in layered oxide cathode materials during battery charging. *Nat. Energy* **2018**, *3*, 641–647. [[CrossRef](#)]
26. Zhang, X.; Belharouak, I.; Li, L.; Lei, Y.; Elam, J.W.; Nie, A.; Chen, X.; Yassar, R.S.; Axelbaum, R.L. Structural and electrochemical study of Al_2O_3 and TiO_2 coated $\text{Li}_{1.2}\text{Ni}_{0.13}\text{Mn}_{0.54}\text{Co}_{0.13}\text{O}_2$ cathode material using ALD. *Adv. Energy Mater.* **2013**, *3*, 1299–1307. [[CrossRef](#)]
27. Zheng, J.; Yang, Z.; Wang, P.; Tang, L.; An, C.; He, Z. Multiple linkage modification of lithium-rich layered oxide $\text{Li}_{1.2}\text{Mn}_{0.54}\text{Ni}_{0.13}\text{Co}_{0.13}\text{O}_2$ for lithium ion battery. *ACS Appl. Mater. Interfaces* **2018**, *10*, 31324–31329. [[CrossRef](#)]
28. Amalraj, F.; Talianker, M.; Markovsky, B.; Burlaka, L.; Leifer, N.; Goobes, G.; Erickson, E.M.; Haik, O.; Grinblat, J.; Zinigrad, E.; et al. Studies of Li and Mn-Rich $\text{Li}_x[\text{MnNiCo}]\text{O}_2$ electrodes: Electrochemical performance, structure and the effect of the aluminum fluoride coating. *J. Electrochem. Soc.* **2013**, *160*, A2220–A2233. [[CrossRef](#)]

29. Nayak, P.K.; Grinblat, J.; Levi, M.; Levi, E.; Kim, S.; Choi, J.W.; Aurbach, D. Al Doping for mitigating the capacity fading and voltage decay of layered Li and Mn-rich cathodes for Li-Ion batteries. *Adv. Energy Mater.* **2016**, *6*, 1502398. [[CrossRef](#)]
30. Chen, G.; An, J.; Meng, Y.; Yuan, C.; Matthews, B.; Dou, F.; Shi, L.; Zhou, Y.; Song, P.; Wu, G.; et al. Cation and anion Co-doping synergy to improve structural stability of Li- and Mn-rich layered cathode materials for lithium-ion batteries. *Nano Energy* **2019**, *57*, 157–165. [[CrossRef](#)]
31. Nayak, P.K.; Grinblat, J.; Levi, M.; Haik, O.; Levi, E.; Aurbach, D. Effect of Fe in suppressing the discharge voltage decay of high capacity Li-rich cathodes for Li-ion batteries. *J. Solid State Electrochem.* **2015**, *19*, 2781–2792. [[CrossRef](#)]
32. Dong, X.; Xu, Y.; Xiong, L.; Sun, X.; Zhang, Z. Sodium substitution for partial lithium to significantly enhance the cycling stability of Li_2MnO_3 cathode material. *J. Power Sources* **2013**, *243*, 78–87. [[CrossRef](#)]
33. Dong, X.; Xu, Y.; Yan, S.; Mao, S.; Xiong, L.; Sun, X. Towards low-cost, high energy density Li_2MnO_3 cathode materials. *J. Mater. Chem. A* **2015**, *3*, 670–679. [[CrossRef](#)]
34. Breddemann, U.; Erickson, E.M.; Davis, V.; Schipper, F.; Ellwanger, M.; Daub, M.; Hoffmann, A.; Erk, C.; Markovsky, B.; Aurbach, D.; et al. Fluorination of Li-rich lithium ion battery cathode materials by fluorine gas: Chemistry, characterization and electrochemical performance in half cells. *ChemElectroChem* **2019**, *3*, 3337–3349. [[CrossRef](#)]
35. Erickson, E.M.; Sclar, H.; Schipper, F.; Liu, J.; Tian, R.; Ghanty, C.; Burstein, L.; Leifer, N.; Grinblat, J.; Talianker, M.; et al. High-temperature treatment of Li-rich cathode materials with ammonia: Improved capacity and mean voltage stability during cycling. *Adv. Energy Mater.* **2017**, *7*, 1700708. [[CrossRef](#)]
36. Shizuka, K.; Kiyohara, C.; Shima, K.; Takeda, Y. Effect of CO_2 on layered $\text{Li}_{1+z}\text{Ni}_{1-x-y}\text{Co}_x\text{Mn}_y\text{O}_2$ (M=Al, Mn) cathode materials for lithium ion batteries. *J. Power Sources* **2007**, *166*, 233–238. [[CrossRef](#)]
37. Sclar, H.; Sicklinger, J.; Erickson, E.M.; Maiti, S.; Grinblat, J.; Talianker, M.; Amalraj, S.F.; Burstein, L.; Beyer, H.; Hartmann, L.; et al. Enhancement of electrochemical performance of lithium and manganese-rich cathode materials via thermal treatment with SO_2 . *J. Electrochem. Soc.* **2020**, *167*, 110563. [[CrossRef](#)]
38. Johnson, C.S.; Kim, J.-S.; Lefief, C.; Li, N.; Vaughey, J.T.; Thackeray, M.M. The significance of the Li_2MnO_3 component in ‘composite’ $x\text{Li}_2\text{MnO}_3 \cdot (1-x)\text{LiMn}_{0.5}\text{Ni}_{0.5}\text{O}_2$ electrodes. *Electrochem. Commun.* **2004**, *6*, 1085–1091. [[CrossRef](#)]
39. Rossouw, M.; Thackeray, M. Lithium manganese oxides from Li_2MnO_3 for rechargeable lithium battery applications. *Mater. Res. Bull.* **1991**, *26*, 463–473. [[CrossRef](#)]
40. Maiti, S.; Sclar, H.; Rosy, Grinblat, J.; Talianker, M.; Burstein, L.; Noked, M.; Markovsky, B.; Aurbach, D. Modification of Li- and Mn-rich cathode materials via formation of the rock-salt and spinel surface layers for steady and high-rate electrochemical performances. *ACS Appl. Mater. Interfaces* **2020**, *12*, 32698–32711. [[CrossRef](#)]
41. Erickson, E.M.; Schipper, F.; Tian, R.; Shin, J.-Y.; Erk, C.; Chesneau, F.F.; Lampert, J.K.; Markovsky, B.; Aurbach, D. Enhanced capacity and lower mean charge voltage of Li-rich cathodes for lithium ion batteries resulting from low-temperature electrochemical activation. *RSC Adv.* **2017**, *7*, 7116–7121. [[CrossRef](#)]
42. Thackeray, M.M.; Kang, S.-H.; Johnson, C.S.; Vaughey, J.T.; Benedek, R.; Hackney, S.A. Li_2MnO_3 -stabilized LiMO_2 (M = Mn, Ni, Co) electrodes for lithium-ion batteries. *J. Mater. Chem.* **2007**, *17*, 3112–3125. [[CrossRef](#)]
43. Shimoda, K.; Yazawa, K.; Matsunaga, T.; Murakami, M.; Yamanaka, K.; Ohta, T.; Matsubara, E.; Ogumi, Z.; Abe, T. Sequential delithiation behavior and structural rearrangement of a nanoscale composite-structured $\text{Li}_{1.2}\text{Ni}_{0.2}\text{Mn}_{0.6}\text{O}_2$ during charge–discharge cycles. *Sci. Rep.* **2020**, *10*, 10048. [[CrossRef](#)] [[PubMed](#)]
44. Croy, J.R.; Gallagher, K.G.; Balasubramanian, M.; Chen, Z.; Ren, Y.; Kim, D.; Kang, S.-H.; Dees, D.W.; Thackeray, M.M. Examining hysteresis in composite $x\text{Li}_2\text{MnO}_3 \cdot (1-x)\text{LiMO}_2$ cathode structures. *J. Phys. Chem. C* **2013**, *117*, 6525–6536. [[CrossRef](#)]
45. Assat, G.; Iadecola, A.; Foix, D.; Dedryvère, R.; Tarascon, J.-M. Direct quantification of anionic redox over long cycling of Li-rich NMC via hard X-ray photoemission spectroscopy. *ACS Energy Lett.* **2018**, *3*, 2721–2728. [[CrossRef](#)]
46. Lu, Z.; Dahn, J.R. Understanding the anomalous capacity of $\text{Li}/\text{Li}[\text{Ni}_x\text{Li}_{(1/3-2x/3)}]\text{Mn}_{(2/3-x/3)}\text{O}_2$ cells using in situ X-Ray diffraction and electrochemical studies. *J. Electrochem. Soc.* **2002**, *149*, A815. [[CrossRef](#)]
47. Yu, D.Y.W.; Yanagida, K.; Kato, Y.; Nakamura, H. Electrochemical Activities in Li_2MnO_3 . *J. Electrochem. Soc.* **2009**, *156*, A417. [[CrossRef](#)]
48. Phillips, P.J.; Bareño, J.; Li, Y.; Abraham, D.P.; Klie, R.F. On the localized nature of the structural transformations of Li_2MnO_3 following electrochemical cycling. *Adv. Energy Mater.* **2015**, *5*, 1501252. [[CrossRef](#)]

49. Francis, A.S.; Markovsky, B.; Sharon, D.; Talianker, M.; Zinigrad, E.; Persky, R.; Haik, O.; Grinblat, J.; Lampert, J.; Schulz-Dobrick, M.; et al. Study of the electrochemical behavior of the “inactive” Li_2MnO_3 . *Electrochim. Acta* **2012**, *78*, 32–39. [[CrossRef](#)]
50. Yu, H.; Ishikawa, R.; So, Y.-G.; Shibata, N.; Kudo, T.; Zhou, H.; Ikuhara, Y. Direct atomic-resolution observation of two phases in the $\text{Li}_{1.2}\text{Mn}_{0.567}\text{Ni}_{0.166}\text{Co}_{0.067}\text{O}_2$ cathode material for lithium-ion batteries. *Angew. Chemie Int. Ed.* **2013**, *52*, 5969–5973. [[CrossRef](#)]
51. Xu, B.; Fell, C.R.; Chi, M.; Meng, Y.S. Identifying surface structural changes in layered Li-excess nickel manganese oxides in high voltage lithium ion batteries: A joint experimental and theoretical study. *Energy Environ. Sci.* **2011**, *4*, 2223–2233. [[CrossRef](#)]
52. Rana, J.; Stan, M.; Kloepsch, R.; Li, J.; Schumacher, G.; Welter, E.; Zizak, I.; Banhart, J.; Winter, M. Structural changes in Li_2MnO_3 cathode material for Li-Ion batteries. *Adv. Energy Mater.* **2014**, *4*, 1300998. [[CrossRef](#)]
53. Chen, H.; Islam, M.S. Lithium extraction mechanism in Li-rich Li_2MnO_3 involving oxygen hole formation and dimerization. *Chem. Mater.* **2016**, *28*, 6656–6663. [[CrossRef](#)]
54. Seo, D.H.; Lee, J.; Urban, A.; Malik, R.; Kang, S.; Ceder, G. The structural and chemical origin of the oxygen redox activity in layered and cation-disordered Li-excess cathode materials. *Nat. Chem.* **2016**, *8*, 692–697. [[CrossRef](#)]
55. Cao, T.; Shi, C.; Zhao, N.; He, C.; Li, J.; Liu, E. Understanding the electrochemical properties of Li-rich cathode materials from first-principles calculations. *J. Phys. Chem. C* **2015**, *119*, 28749–28756. [[CrossRef](#)]
56. Lee, E.; Persson, K.A. Structural and chemical evolution of the layered Li-excess Li_xMnO_3 as a function of Li content from first-principles calculations. *Adv. Energy Mater.* **2014**, *4*, 1400498. [[CrossRef](#)]
57. Zhang, Z.; Zhao, S.; Wang, B.; Yu, H. Local redox reaction of high valence manganese in Li_2MnO_3 -based lithium battery cathodes. *Cell Rep. Phys. Sci.* **2020**, *1*, 100061. [[CrossRef](#)]
58. Amalraj, S.F.; Sharon, D.; Talianker, M.; Julien, C.M.; Burlaka, L.; Lavi, R.; Zhecheva, E.; Markovsky, B.; Zinigrad, E.; Kovacheva, D.; et al. Study of the nanosized Li_2MnO_3 : Electrochemical behavior, structure, magnetic properties, and vibrational modes. *Electrochim. Acta* **2013**, *97*, 259–270. [[CrossRef](#)]
59. Sekar, M.M.A.; Patil, K.C. Combustion synthesis and properties of fine-particle dielectric oxide materials. *J. Mater. Chem.* **1992**, *2*, 739–743. [[CrossRef](#)]
60. Hershkovitz, S.; Baltianski, S.; Tsur, Y. Electrochemical impedance analysis of SOFC cathode reaction using evolutionary programming. *Fuel Cells* **2012**, *12*, 77–85. [[CrossRef](#)]
61. Oz, A.; Gelman, D.; Goren, E.; Shomrat, N.; Baltianski, S.; Tsur, Y. A novel approach for supercapacitors degradation characterization. *J. Power Sources* **2017**, *355*, 74–82. [[CrossRef](#)]
62. Kalimuthu, V.S.; Attias, R.; Tsur, Y. Electrochemical impedance spectra of RuO_2 during oxygen evolution reaction studied by the distribution function of relaxation times. *Electrochem. Commun.* **2020**, *110*, 106641. [[CrossRef](#)]
63. Kraus, W.; Nolze, G. POWDER CELL—A program for the representation and manipulation of crystal structures and calculation of the resulting X-ray powder patterns. *J. Appl. Crystallogr.* **1996**, *29*, 301–303. [[CrossRef](#)]
64. Rodríguez-Carvajal, J. Recent advances in magnetic structure determination by neutron powder diffraction. *Phys. B Condens. Matter* **1993**, *192*, 55–69. [[CrossRef](#)]
65. Gabrisch, H.; Yi, T.; Yazami, R. Transmission electron microscope studies of $\text{LiNi}_{1/3}\text{Mn}_{1/3}\text{Co}_{1/3}\text{O}_2$ before and after long-term aging at 70 °C. *Electrochem. Solid-State Lett.* **2008**, *11*, A119. [[CrossRef](#)]
66. Ravel, B.; Newville, M. ATHENA, ARTEMIS, HEPHAESTUS: Data analysis for X-ray absorption spectroscopy using IFEFFIT. *J. Synchrotron Radiat.* **2005**, *12*, 537–541. [[CrossRef](#)]
67. Julien, C.M.; Massot, M. Lattice vibrations of materials for lithium rechargeable batteries III. Lithium manganese oxides. *Mater. Sci. Eng. B* **2003**, *100*, 69–78. [[CrossRef](#)]
68. Strobel, P.; Lambert-Andron, B. Crystallographic and magnetic structure of Li_2MnO_3 . *J. Solid State Chem.* **1988**, *75*, 90–98. [[CrossRef](#)]
69. Ye, D.; Sun, C.; Chen, Y.; Ozawa, K.; Hulicova-Jurcakova, D.; Zou, J. Ni-induced stepwise capacity increase in Ni-poor Li-rich cathode materials for high performance lithium ion. *Nano Res.* **2015**, *8*, 808–820. [[CrossRef](#)]
70. Teufl, T.; Strehle, B.; Müller, P.; Gasteiger, H.A.; Mendez, M.A. Oxygen release and surface degradation of Li- and Mn-rich layered oxides in variation of the Li_2MnO_3 content. *J. Electrochem. Soc.* **2018**, *165*, A2718–A2731. [[CrossRef](#)]
71. Strehle, B.; Kleiner, K.; Jung, R.; Chesneau, F.; Mendez, M.; Gasteiger, H.A.; Piana, M. The role of oxygen release from Li- and Mn-rich layered oxides during the first cycles investigated by on-line electrochemical mass spectrometry. *J. Electrochem. Soc.* **2017**, *164*, A400–A406. [[CrossRef](#)]

72. Muhammad, S.; Kim, H.; Kim, Y.; Kim, D.; Song, J.H.; Yoon, J.; Park, J.-H.; Ahn, S.-J.; Kang, S.-H.; Thackeray, M.M.; et al. Evidence of reversible oxygen participation in anomalously high capacity Li- and Mn-rich cathodes for Li-ion batteries. *Nano Energy* **2016**, *21*, 172–184. [[CrossRef](#)]
73. Saubanère, M.; McCalla, E.; Tarascon, J.-M.; Doublet, M.-L. The intriguing question of anionic redox in high-energy density cathodes for Li-ion batteries. *Energy Environ. Sci.* **2016**, *9*, 984–991. [[CrossRef](#)]
74. Rozier, P.; Tarascon, J.M. Review—Li-rich layered oxide cathodes for next-generation Li-Ion batteries: Chances and challenges. *J. Electrochem. Soc.* **2015**, *162*, A2490–A2499. [[CrossRef](#)]
75. Chen, Q.; Pei, Y.; Chen, H.; Song, Y.; Zhen, L.; Xu, C.-Y.; Xiao, P.; Henkelman, G. Highly reversible oxygen redox in layered compounds enabled by surface polyanions. *Nat. Commun.* **2020**, *11*, 3411. [[CrossRef](#)] [[PubMed](#)]
76. Ohzuku, T.; Nagayama, M.; Tsuji, K.; Ariyoshi, K. High-capacity lithium insertion materials of lithium nickel manganese oxides for advanced lithium-ion batteries: Toward rechargeable capacity more than 300 mAhg⁻¹. *J. Mater. Chem.* **2011**, *21*, 10179–10188. [[CrossRef](#)]
77. Watanabe, A.; Matsumoto, F.; Fukunishi, M.; Kobayashi, G.; Ito, A.; Hatano, M.; Ohsawa, Y.; Sato, Y. Relationship between electrochemical pre-treatment and cycle performance of a Li-rich solid-solution layered Li_{1-α}[Ni_{0.18}Li_{0.20+α}Co_{0.03}Mn_{0.58}]O₂ cathode for Li-Ion secondary batteries. *Electrochemistry* **2012**, *80*, 561–565. [[CrossRef](#)]
78. Ito, A.; Li, D.; Ohsawa, Y.; Sato, Y. A new approach to improve the high-voltage cyclic performance of Li-rich layered cathode material by electrochemical pre-treatment. *J. Power Sources* **2008**, *183*, 344–346. [[CrossRef](#)]
79. Ito, A.; Li, D.; Sato, Y.; Arao, M.; Watanabe, M.; Hatano, M.; Horie, H.; Ohsawa, Y. Cyclic deterioration and its improvement for Li-rich layered cathode material Li[Ni_{0.17}Li_{0.2}Co_{0.07}Mn_{0.56}]O₂. *J. Power Sources* **2010**, *195*, 567–573. [[CrossRef](#)]
80. Van Bommel, A.; Krause, L.J.; Dahn, J.R. Investigation of the irreversible capacity loss in the lithium-rich oxide Li[Li_{1/5}Ni_{1/5}Mn_{3/5}]O₂. *J. Electrochem. Soc.* **2011**, *158*, A731. [[CrossRef](#)]
81. Wills, A.S.; Raju, N.P.; Greedan, J.E. Low-temperature structure and magnetic properties of the spinel LiMn₂O₄: A frustrated antiferromagnet and cathode material. *Chem. Mater.* **1999**, *11*, 1510–1518. [[CrossRef](#)]
82. Nakashima, S.; Nakatake, Y.; Harima, H.; Katsuno, M.; Ohtani, N. Detection of stacking faults in 6H-SiC by Raman scattering. *Appl. Phys. Lett.* **2000**, *77*, 3612–3614. [[CrossRef](#)]
83. Leifer, N.; Schipper, F.; Erickson, E.M.; Ghanty, C.; Talianker, M.; Grinblat, J.; Julien, C.M.; Markovsky, B.; Aurbach, D. Studies of spinel-to-layered structural transformations in LiMn₂O₄ electrodes charged to high voltages. *J. Phys. Chem. C* **2017**, *121*, 9120–9130. [[CrossRef](#)]
84. Amalraj, S.F.; Burlaka, L.; Julien, C.M.; Mauger, A.; Kovacheva, D.; Talianker, M.; Markovsky, B.; Aurbach, D. Phase Transitions in Li₂MnO₃ electrodes at various states-of-charge. *Electrochim. Acta* **2014**, *123*, 395–404. [[CrossRef](#)]
85. Maruszczyk, A.; Albina, J.-M.; Hammerschmidt, T.; Drautz, R.; Eckl, T.; Henkelman, G. Oxygen activity and peroxide formation as charge compensation mechanisms in Li₂MnO₃. *J. Mater. Chem. A* **2017**, *5*, 15183–15190. [[CrossRef](#)]
86. Kantcheva, M.; Kucukkal, M.; Suzer, S. XPS and IR characterization of manganese ions deposited on alumina. *J. Mol. Struct.* **1999**, *482–483*, 19–22. [[CrossRef](#)]

